Investigation and Development of CO_2 Gas Sensors

Based on Perovskite Oxides

by

Zeynep Sena Kulaksız

A Dissertation Submitted to the
Graduate School of Sciences and Engineering
in Partial Fulfillment of the Requirements for
the Degree of

Master of Science

in

Chemistry

August 21, 2020

Investigation and Development of CO_2 Gas Sensors Based on Perovskite Oxides

Koç University

Graduate School of Sciences and Engineering

This is to certify that I have examined this copy of a master's thesis by

Zeynep Sena Kulaksız

and have found that it is complete and satisfactory in all respects,
and that any and all revisions required by the final
examining committee have been made.

Committee Members:

Assoc. Prof. Uğur Ünal (Advisor)

Prof. Esma Sezer

Asst. Prof. Umut Aydemir

Date: 21.08.2020

To my mom, she always be my light,

ABSTRACT

Investigation and Development of CO_2 Gas Sensors Based on Perovskite Oxides

Zeynep Sena Kulaksız

Master of Science in Chemistry

August 21, 2020

The need for energy rapidly increased with the development of humanity and technology. The required energy has been mainly provided by fossil fuels such as coal, natural gas, and oil. However, these sources are limited and nonrenewable. Additionally, massive consumption of these sources is causing environmental problems like global warming via the greenhouse effect. Increased CO_2 ratio in the atmosphere is causing solar energy adsorption and keep the heat close to the Earth's surface. Furthermore, CO_2 is used for many purposes in daily life such as in refrigerators, fire extinguishers, carbonated drinks, or manufacturing processes. Thus, CO_2 has crucial role on carbon cycle which is necessary for the living creatures and the Earth, but it harms human health when it is not properly handled.

It is highly important to control the level of CO_2 in the environment for comfort and health. Thus, main purpose of this study is to develop chemiresistive CO_2 sensing materials and manufacture highly efficient and low-cost sensor and also another the synthesis and characterization of ABO_3 type perovskites and examine them as CO_2 sensing materials.

In the presented work, $LaMnO_3$ and $LaTiO_3$ based undoped and doped perovskites were prepared with sol-gel method and the films of these perovskites were examined for CO_2 sensing. Film were deposited with electrophoretic deposition and spin coating methods. Material characterization was performed with various techniques such as X-ray diffraction (XRD), X-ray fluorescence (XRF), and scanning electron microscopy (SEM).

Porous structure and surface area of the powders were the most important parameters for a good sensing material. Thus, the dopant ratio and dopant type were examined carefully with homemade sensing setup to obtain the best working sensing material. Also, gas sensing properties were studied different parameters like temperature, and gas concentration to obtain optimum conditions.

ÖZETÇE

Perovskit Oksitlere Dayalı CO_2 Gaz Sensörlerinin Araştırılması ve Geliştirilmesi

Zeynep Sena Kulaksız

Kimya, Yüksek Lisans

21 Ağustos 2020

İnsanlığın ve teknolojinin gelişmesiyle birlikte enerji ihtiyacı hızla artmıştır. Gerekli enerji büyük oranda, kömür, doğal gaz ve petrol gibi fosil yakıtlardan sağlanmaktadır. Ancak, bu kaynaklar sınırlıdır ve yenilenemezler. Ek olarak, bu kaynakların yoğun tüketimi, sera etkisiyle küresel ısınma gibi çevresel sorunlara neden olmaktadır. Atmosferdeki artan CO_2 oranı, güneş enerjisi emilimine neden olur ve ısıyı Dünya'nın yüzeyine yakın tutar. Dahası, CO_2 günlük hayatta buzdolaplarında, yangın söndürücülerde, gazlı içeceklerde veya üretim işlemleri gibi birçok amaç için kullanılır. Canlılar ve Dünya için gerekli olan karbon döngüsü üzerinde önemli bir role sahiptir ancak uygun şekilde kullanılmadığında insan sağlığı üzerinde olumsuz etkisi vardır.

CO_2 gazının yaygın kullanımı ışığında, bu çalışmanın temel amacı ABO_3 tipi perovskitlerin sentezi ve karakterizasyonu olup bunları CO_2 algılama materyali olarak incelemektir. Ayrıca yüksek verimli ve düşük maliyetli sensor üretmektir.

Konfor ve sağlık için ortamdaki CO_2 seviyesinin kontrol edilmesi son derece önemlidir. Bu nedenle, bu çalışmanın temel amacı, kimyasallara dirençli CO_2 algılama malzemeleri geliştirmek ve yüksek verimli ve düşük maliyetli sensör üretmektir. Amaç, ABO3 tipi perovskitlerin sentezi ve karakterizasyonu ve bunları CO_2 algılama malzemeleri olarak incelemektir.

Sunulan çalışmada, $LaMnO_3$ ve $LaTiO_3$ bazlı katkısız ve katkılı perovskitler sol-jel yöntemi ile hazırlanmıştır ve bu perovskitlerin filmleri CO_2 algılama açısından incelenmiştir. Film, elektroforetik biriktirme ve döndürerek kaplama yöntemleri ile kaplanmıştır. Malzeme karakterizasyonu, X-ışını kırınımı (XRD), X-ışını flüoresansı (XRF) ve taramalı elektron mikroskobu (SEM) gibi çeşitli tekniklerle gerçekleştirilmiştir.

Tozların gözenekli yapısı ve yüzey alanı, iyi bir algılama malzemesi için en önemli parametrelerdir. Bu nedenle, katkı maddesi oranı ve katkı maddesi türü, en iyi çalışan algılama malzemesini elde etmek için ev yapımı algılama sistemiyle dikkatlice incelenmiştir. Ayrıca, optimum koşulları elde etmek için gaz algılama özellikleri sıcaklık ve gaz konsantrasyonu gibi farklı parametreler üzerinde çalışılmıştır.

AKNOWLEDGEMENTS

I would like to express my sincere gratitude to all the people who have supported and helped me during my master study.

I would like to offer my endless thanks to my advisor Assoc. Prof. Uğur ÜNAL and Dr. Ceren YILMAZ AKKAYA giving me the opportunity to work with them and seeing my potential. I am very grateful to be a part of the Uğur Ünal Research Lab. During my research, I have learned that asking questions and consulting without hesitation is essential and thanks to Dr.ÜNAL patience, optimism, vast knowledge, and versatility, my questions never stayed unanswered and I am able to discover my future interests. I have to specially thank to Dr.AKKAYA, because she put her heart and mind in this project.

Also, I am thankful to Dr. Durata HACIU ERTEK for supporting the project and being a kind and a helpful teacher and KUYTAM members to their patience and guidance.

I would also like to thank my thesis committee, Prof. Esma SEZER and Asst. Prof. Umut AYDEMIR, for their kind support, contributions, and time. Especially, I am very indebted to my undergraduate advisor Prof. Esma SEZER because I have learned so many valuable lessons from her not only academically but also about life.

For last few year, I spent most of my time with my dearest friends Eda KARAMAN, Gizem SONGUR, Merve TAŞER, Sema TOPAL and Zahide ASKEROĞLU. They had been with me as the biggest supporters and as sisters. Even in our worst times, joy and laughter have always been and will continue to exist.

Also, I feel very lucky and happy to find and be friend with Hüseyin KÜÇÜKKEÇECİ, Merve ERCAN, Sultan ÇETİN and Yaşar Can AYRA. My time in Koç University became more meaningful and enjoyable. I will very miss every second that we spent together.

Especially, I have to thank my housemates Sebahat TOPAL and Sema TOPAL. They are my biggest support in these two years. We laughed, cried, and learnt together. The moment I got home, my mood would go up immediately. I will miss you very much.

Finally, I could not have achieved my current level of success without my mother, Nazan ÜSTÜNKÖY, who supported me with all her love and understanding. She put her all effort for me to create a better future and life. I have always admired and exemplified her strength, determination, intelligence, diligence, and humour. I am very lucky to have her.

TABLE OF CONTENTS

LIST OF TABLES

LIST OF FIGURES

ABBREVIATIONS

DFT	: Density Function Theory
IDE	: Interdigitated Electrode
LMO	: LaMnO3
LMO-Ca	: Calcium doped $LaMnO_3$
LMO-Co	: Cobalt doped $LaMnO_3$
LMO-Fe	: Iron doped $LaMnO_3$
LMO-Ni	: Nickel doped $LaMnO_3$
LTO	: $LaTiO_3$
LTO-Ca	: Calcium doped $LaTiO_3$
LTO-Co	: Cobalt doped $LaTiO_3$
LTO-Fe	: Iron doped $LaTiO_3$
LTO-Ni	: Nickel doped $LaTiO_3$
LTO-Sr	: Strontium doped $LaTiO_3$
SEM	: Scanning Electron Microscopy
XRD	: X-Ray Diffraction Spectroscopy
XRF	: X-Ray Fluorescence Spectroscopy

Chapter 1:
INTRODUCTION

1.1 Perovskite Materials

Perovskite is used to describe $CaTiO_3$ like oxides that have a general formula such as ABO_3 or A_2BO_4 which was discovered by German scientist Gustav Rose in the Ural Mountains in 1839. The A site cation is 12-fold coordinated and the B site cation is 6-fold coordinated with the oxygen anions which forms an cubic lattice as showed in Figure 1-1 [1],[2]. B is generally a metal cation which forms BO_6 octahedral structure with oxygen anion and A metal cation fills the hole between the octahedrons and provides a charge balance[3].

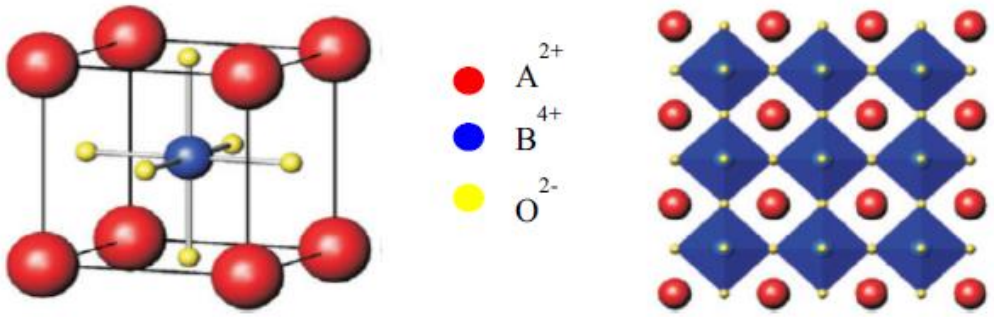

Figure 1-1 : The structure of ABO_3 type and an ideal cubic perovskite [4]

In an ideal structure, if cubic unit cell parameter defined as a, B-O distance is a/2 and A-O distance is a/√2, Eq.1.1 can be applicable.

$$(r_A + r_O) = [\sqrt{2}(r_B + r_O)] \quad (1.1)$$

However, non-ideal structures do not follow this rule, so Goldschmidt presented a tolerance factor (t) by using ionic radii model. In the ionic radii model, the ions were treated as charged, rigid and non-polarizable atoms for predicting whether material would form and what structure and symmetry it would have. t is defined by Eq. 1.2.

$$t = (r_A + r_O)/[\sqrt{2}(r_B + r_O)] \quad (1.2)$$

$$0.75 \leq t \leq 1$$

where t is tolerance factor, and r_A, r_B, and r_O are the radii of A element, B element, and oxygen, respectively in the perovskite structure. This formula is applicable at room temperature.

An ideal cubic structure appears in few cases at high temperatures, where t value is 1. For highly dielectric or ferroelectric materials, tolerance factor is more than 1. In most cases, tolerance factor is lower than 1 and the materials display low symmetries. Moreover, the studies proved that true symmetry of naturally occurred $CaTiO_3$ is orthorhombic not cubic [5], [6].

As electronegativities and ionic radii of A and B site cations change, lattice parameters change and the structure of the unit cell gets distorted to lower symmetry structures that create point defects like oxygen vacancies and electrons [7]. Due to the distortion, essential physical properties like dielectric, magnetic and electronic can differ and give rise to diverse applications such as sensing material, batteries, photocatalyst, etc.[3].

1.2 Physical and Chemical Properties of Perovskites

Perovskites display many different characters related to their structures and formations like electroneutrality and ionic radii. They can form various chemical compositions with numerous elements and compounds (Figure 1-2). By variation of A-site and B-site cation composition, properties like band structure or charge transfer can be engineered [8],[9]. Transition metals are used to modify the electronic structure as the B site metal determines the conduction band level. Alkali or alkali earth metals are used to control the structure, and they have a small effect on electronic structure.

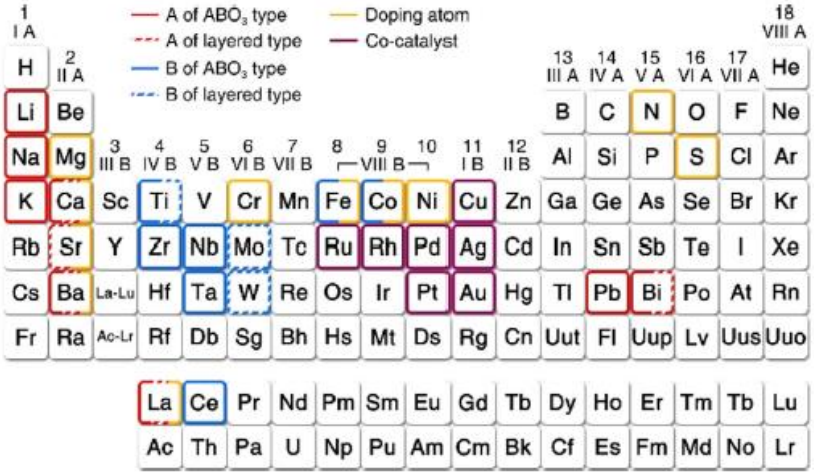

Figure 1-2 : Elements that used for forming perovskite oxides [9]

Table 1-1 lists several properties and related compounds. As seen in the table, perovskites find a wide range of applications due their properties. [8].

Table 1-1 : Typical properties of perovskite oxides [5]

Typical property	Typical compound
Ferromagnetic property	$BaTiO_3$, $PdTiO_3$
Piezoelectricity	$Pb(Zr, Ti)O_3$, $(Bi, Na)TiO_3$
Electrical conductivity	ReO_3, $SrFeO_3$, $LaCoO_3$, $LaNiO_3$, $LaCrO_3$
Superconductivity	$La_{0.9}Sr_{0.1}CuO_3$, $YBa_2Cu_3O_7$, $HgBa_2Ca_2Cu_2O_8$
Ion conductivity	$La(Ca)AlO_3$, $CaTiO_3$, $La(Sr)Ga(Mg)O_3$, $BaZrO_3$, $SrZrO_3$, $BaCeO_3$
Magnetic property	$LaMnO_3$, $LaFeO_3$, La_2NiMnO_6
Catalytic property	$LaCoO_3$, $LaMnO_3$, $BaCuO_3$
Electrode	$La_{0.6}Sr_{0.4}CoO_3$, $La_{0.8}Ca_{0.2}MnO_3$

1.2.1 Electrical and Magnetic Properties

Perovskite materials have different types of conductivities. Some of them shows dielectric properties like ferroelectricity, piezoelectricity, electrostriction, and pyroelectricity, some shows metallic conductivity [8]. Their electrical properties are dependent the outermost electrons. Because these electrons may localize at specific atomic sites and may bear spontaneous momentum causing a change in their behavior. As an exemplary, low state Ni^{III} contain $LaNiO_3$ (semiconductor) shows metallic conductivity and Pauli paramagnetism [5].

Dielectric materials can preserve electro-static field for a long time. They display great resistance to electrical current so perovskite with this feature used in capacitors to improve the performance [4]. One of the most popular ferroelectric material is $BaTiO_3$. It has been studied vastly for various applications. The dielectric behavior is explained with its altering crystal structure (monoclinic to tetragonal to cubic) and dependence on the temperature. For example above 303 K, cubic $BaTiO_3$ shows no ferroelectricity but has high dielectric constant [10].

Superconductivity of cuprates gained popularity since its discovery in 1986 and electrical properties of perovskites subjected to many research [5]. Cu on the B site was found to be essential for the occurrence of superconductivity. Also research showed that critical temperature depends on Cu-O layers in the crystal structure [10].

In ABO_3 ideal perovskite structure, two B^{3+} ions share an oxygen atom and B-O-B bond is formed which causes an antiparallel coupling of magnetic moments. If B' is a diamagnetic ion, B^{3+} ions in $A_2BB'O_6$ sublattice are aligned antiferromagnetically [5].

1.2.2 Catalytic Activity

Perovskites display high catalytic activity and stability because they have large number of oxygen vacancies in their structure. These vacancies lead to oxygen reduction or oxygen activation which rendered them as valuable catalyst in the automobile industry and environmental applications. Furthermore, they are used as an alternative to precious metal containing catalyst [8], [10]

It was reported that Cu, Co, Fe, or Mn containing perovskite oxides exhibited superb activity upon direct decomposition of NO at high temperatures. Secondly, they display excellent performance as an intelligent (self-regenerated) automobile catalyst for emission control. To reduce the amount of precious metals that used, fine particles with consisting of high surface-to-volume ratio would be chosen. However, these particles can be unstable at operating conditions so perovskite oxide containing fine particles like $LaFe_{0.57}Co_{0.38}Pd_{0.05}O_3$ material is used and provide high dispersion of Pd [4], [10],[11].

Another vastly studied topic is photocatalysis and photoelectrocatalysis. Light harvesting and redox capability are important aspects for efficient photocatalyst. For this reason, perovskites such as $SrTiO_3$ or $NaTaO_3$ are highly studied. Also, perovskites are prone to band gap engineering which make them excellent choice for CO_2 reduction and water splitting applications [12].

1.3 Synthesis Methods for Perovskites

Perovskite materials can be synthesized using conventional or modern techniques. Choosing the right synthesis method is crucial because it has been determined that for a specific compound, different methods results in distinct oxygen permeation flux values, electronic and ionic conduction, particle size, surface area, etc., under the same experiment conditions [13]. Sol-gel (Pechini), solid state reaction, hydrothermal methods and co-precipitation methods are widely used perovskite synthesis. The other existing methods are spray and freeze drying, physical vapor deposition (PVD), spray pyrolysis, combustion synthesis, and microwave assisted synthesis [13].

1.3.1 Sol-gel (Pechini) Method

Sol-gel method is one of the most widely used methods for oxide synthesis. It is a wet chemical method, which allows high purity oxide powder and control of the structure.

Ebelman was the first to report in 1845, slow hydrolysis of ester of silicic acid lead to transparent material. Geffcan and Berger from Shott Company succeeded to obtain sol-gel process for oxide layers in 1930. Following them, D.Roy and R.Roy suggested a different method for more homogenous melts and glass using sol-gel process. In early 60's, some research was conduct but real interest rose in 19^{th} century [14].

The transformation of liquid precursor to colloidal suspension through hydrolysis and condensation of metal alkoxide precursors is called 'sol' formation. The conversion of sol to a covalent network structure is finalized with 'gel' formation. Figure 1-3 summarizes five fundamental gel type [15].

Type of gel	Bonding	Source	Gel schematic
Colloidal[7]	Particles connected by Van der Waals or hydrogen bonding	Metal oxide or hydroxide sols	
Metal-oxane polymer[4]	Inorganic polymers interconnected via covalent or intermolecular bonding	Hydrolysis and condensation of metal alkoxides e.g. SiO_2 from tetramethyl orthosilicate	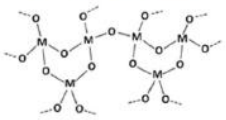
Metal complex[8]	Weakly interconnected metal complexes	Concentrated metal complex solution e.g. aqueous metal citrate or ethanolic metal urea Often form resins or glassy solids rather than gels	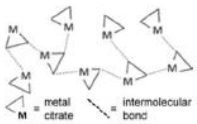
Polymer complex I *In situ* polymerizable complex ('Pechini' method)[9,10]	Organic polymers interconnected by covalent and coordinate bonding	Polyesterification between polyhydroxy alcohol (e.g. ethylene glycol) and carboxylic acid with metal complex (e.g. metal-citrate)	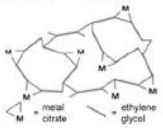
Polymer complex II Coordinating and crosslinking polymers[11]	Organic polymers interconnected by coordinate and intermolecular bonding	Coordinating polymer (e.g. alginate) and metal salt solution (typically aqueous)	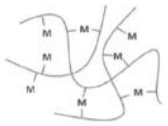

Figure 1-3 : Five type of gel necessary for sol-gel synthesis of materials [11]

In 1967, Pechini described a modified method involving chelating ligands at initial step forming a homogeneous solution of metal/citrate complexes and entrapping the metal ions into a polymer network to gain control over the polymerization process[15].

The initial step is forming a metal-citrate chelate complex by dissolving metal salts and citric acid in a solvent and starting polyesterification reaction by heating after adding ethylene glycol to construct a polymer network (Figure 1-4). Later, the material is carbonized to dispose organic matrix and calcinated at high temperatures [15].

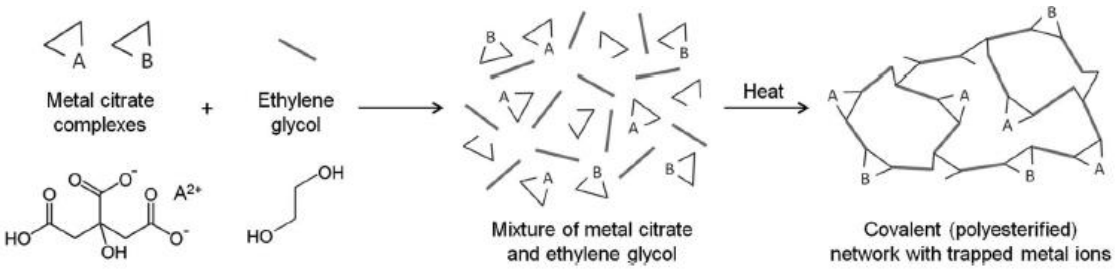

Figure 1-4 : Scheme of Pechini method [11]

Generally, Pechini synthesis results in agglomerated crystallites. However sometimes metal nitrates were used in initial mixture and nitrous oxide was released leading the foam formation. Also, Pechini precursors can use to make thin film or polycrystalline wires [15].

In the coming years, many scientists developed and modified the method for enhancing material and structure range. Mostly, citric acid was exchanged with di-, tri- or tetracarboxylic acids or ethylene glycol with the polyols. Figure 1-5 can be shown as an example the effect of changing ratios of the citric acid and ethylene glycol [15].

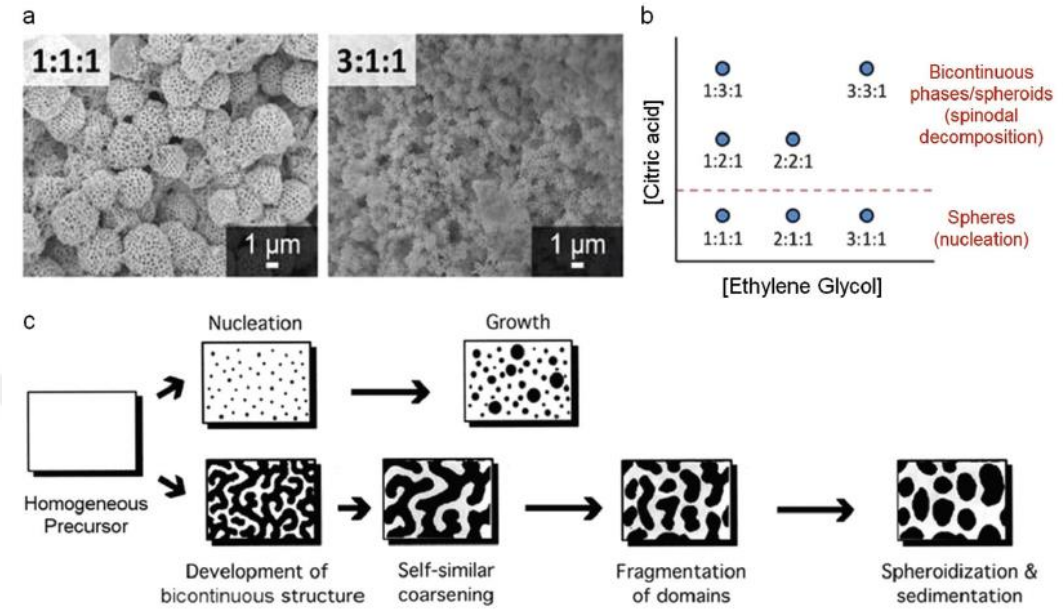

Figure 1-5 : Effect of changing the ratios can be seen a) SEM images with molar ratios ethylene glycol: citric acid: total metal cation b) schematic representation of ratios c) schematic representation of nucleation and spinal decomposition [11]

1.3.2 Solid State Reaction

Solid state reaction method is the most common and one of the oldest synthesis routes for perovskite preparation. In this method, carbonates, salts, or oxide powders were mixed mechanically then treated at high temperatures for several hours for sintering process which let to cations move to the crystalline grains. During reaction, ions diffuse from bulk to interface between particles which affect crystallinity and particle size [13].

High temperature is needed for solid state reaction because the reaction is diffusion limited. Solid state reaction is not effective as sol-gel or Pechini methods in terms of powder quality because it may result in loss of some reactants, may not get desired structure and purity, etc. Reaction only happens at contact points between grains of reactants, following nucleation and growth of a product after the diffusion takes place. Figure 1-6 explains the reaction with visual example [16].

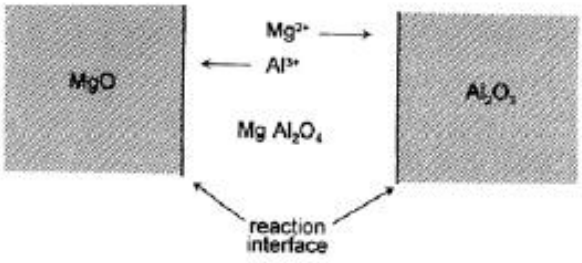

Figure 1-6 : $MgAl_2O_4$ formation using MgO and Al_2O_3 compounds with solid state synthesis [12]

1.3.3 Hydrothermal Method

Hydrothermal method combines the boiling point of aqueous solvent, generally water, and the critical temperature of material at pressures more prominent than 1 atm in a close system called as autoclave like in Figure 1-7 so as to dissolve and recrystallize the materials which are moderately insoluble in water. Crystalline powders can obtain without further calcination by using hydrothermal method.

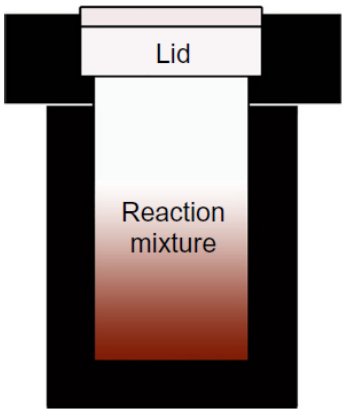

Figure 1-7 : The scheme of Teflon-lined (white part) stainless steel autoclave (black part) [17]

The system consists of three main phases: oil phase, aqueous phase, and surfactant phase. Nanoparticles growth takes place in reaction medium (water). Therefore, reaction medium is heavily affected from temperature, pressure, pH, and reaction time. Also, these conditions allow to adjust particle size and shape modification as wanted [13], [18].

1.3.4 Co-precipitation Method

The co-precipitation method based on high degree of homogeneity of precursors. In this useful technique, a normally soluble component and a macro-component from the same solution were precipitate simultaneously to form mixed crystals as can be seen in Figure 1-8.

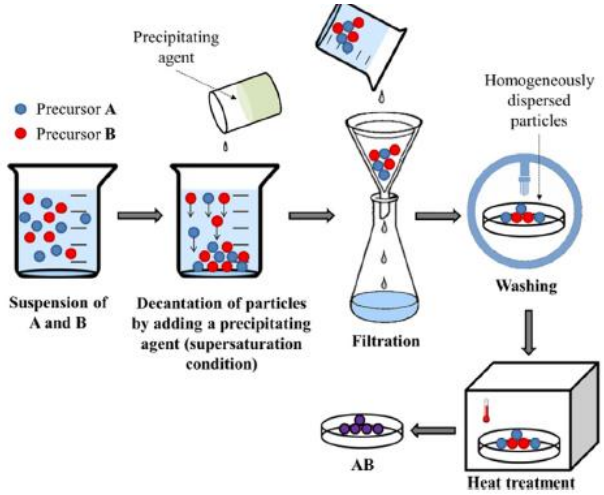

Figure 1-8 : General representation of co-precipitation method [13]

The controllable release of ions helped to gain control over the nucleation and particle growth kinetic but controlling particle size and its distribution is more complicated so by using surfactants or sonochemial method, morphology can be regulated. Moreover several parameter like pH, temperature, concentration and mixing rate are important for the controllable precipitation process and purity of the particle. [12], [13], [17].

1.4 Application of Perovskite Type Materials

For many different practical and model applications, perovskite materials were preferred due to their unique physical and chemical properties. They are used as thin film capacitor, photoelectrochemical cell, sensors, actuators, transducers, drug delivery systems, laser application and catalyst in the chemical industry [19]. The real use of perovskites in industry generally based on its dielectric, ferroelectric, piezoelectric, and pyroelectric properties as seen in Figure 1-9 [20].

Materials	Properties	Applications
$BaTiO_3$	Dielectric	Capacitor, sensor
$(Ba, Sr)TiO_3$	Pyroelectric	Pyrodetector
$PbTiO_3$	Pyroelectric	Pyrodetector
	Piezoelectric	Acoustic transducer
$Pb(Zr, Ti)O_3$	Dielectric	Nonvolatile memory
	Dielectric	Pyrodetector
	Piezoelectric	Surface acoustic wave device, substrate
	Electro-optic	Waveguide device
$(PB, la)(Zr, Ti)O_3$	Pyroelectric	Pyrodetector
	Electro-optic	Waveguide device, optical memory display
$LinbO_3$	Piezoelectric	Pyrodetector, surface acoustic wave device
$LinbO_3/Ti$	Electro-optic	Waveguide device, optic modulator, second harmonic generation
$K(Ta, Nb)O_3$	Pyroelectric	Pyrodetector
	Electro-optic	Waveguide device, frequency doubler
$Pb(Mg_{1/3}Nb_{2/3})O_3$	Dielectric	Memory, capacitor

Figure 1-9 : Properties and applications of perovskite materials [16]

There is a growing interest for perovskites as environmental catalyst. Due to the harmful effect of greenhouse gases, their decomposition and combustion to non-harmful substances gain importance. For example, $LaCoO_3$, $CaMn_{0.7}Cu_{0.3}O_3$ and $La_{0.8}Ba_{0.2}MnO_3$ perovskites used as catalyst successfully for this purpose [12].

Perovskite materials gain popularity in the sensor field. They may be used in gas sensor biosensor (glucose and neurotransmitter), electrochemical sensing of alcohols, acetone and H_2O_2 due to their excellent thermal stability, ideal band gap, controllable semiconductive properties with type of dopant and difference in size on A- and B-sites[8].

Fuel cells have come into see as proficient options to combustion motors because of their potential to play down the natural impact of the utilize of fossil powers. A fuel cell acts like battery converting chemical energy into electrical energy. They have many advantages like zero noise pollution, good efficiency, low emission, modular nature, and future hydrogen fuel economy. They vary based on operating temperature, fuel type, mobile ions, and electrolyte type. Perovskite materials used in solid oxide fuel cells (SOFCs) and exhibits good electronic conductivity, ionic conductivity, thermal, chemical stability, and high catalytic activity. According the their type and character, perovskite oxides can be anode or cathode cell material [8].

1.5 Gas Sensors

1.5.1 Gas Sensors History

In the 1920, the miners used the canary in a cage for sensing poisonous gases like CO, methane etc. relying its natural senses toward the gases. When the canary stops warbling, miners left the mine immediately. In the following years, inventions like Davey's lamp was used but the first real progress happened in 1953, Brattain and Bardeen proposed semiconductors as gas sensitive material. They used Ge based material and observe its resistivity change during contact with the air. Later, Heiland described semiconductor-based sensor for oxygen or other atmospheric gases but further research was not conducted. In 1967, Shaver shared a discovery of the effect of noble metal addition on semiconductors' selectivity and sensitivity which has driven the research on semiconductor gas sensors. At the beginning of 1970s, Taguchi Figaro studied metal oxide materials and made first industrial product. He made sensor using porous SnO_2 with Pd catalyst. Figaro Inc. commercialized the device to prevent fire and accidents. After this breakthrough, sensors gain popularity and developments were made for more sensitive, low cost, smaller, lighter, better specific devices [21],[22].

1.5.2 Gas Sensors

Semiconductor metal oxide gas sensors can be classified by several parameter as metal type (n or p-type), working principle or mechanism (electrical, chemiresistive, calorimetric, optical or capacitance based) [22].

Material type

Gas sensors can be developed from two group of semiconductors: oxide or non-oxides. Non-oxide semiconductors are coated with a protective insulation layer which prevent them act as receptor. On the contrary, oxide semiconductors can work as both receptor and transducer which transforms changing properties effect to electrical signals [23].

Oxide semiconductors can be grouped as n-type and p-type. When they are exposed to target gas their resistance increases or decreases. For n-type semiconductors such as SnO_2, WO_3, and ZnO, diminished resistance was observed with inflammable and reducing gas in air (inorganic: H_2, CO, NH_3, H_2S, NO, etc.; organic: CH_4, propane, alcohols, odorants, etc.). On the contrary, exposure the oxidative gases (NO_2 , ozone,

N_2 O, etc.) causes elevated resistance. Beside redox-active gases CO_2 and water vapor affect the resistance greater or lesser degree [23].

Working Principle

Metal oxide semiconductor (MOS) gas sensor based on resistance change which is caused from adsorption of gas molecule. When the gas is absorbed on the surface, it captures free electrons and depletion layer forms. Electron movements on the depletion layer determine sensing [24].

Electrochemical gas sensors monitor concentration or partial pressure of target gas at electrode and measures the resulting current. Simplest electrochemical cell has two electrode system as seen in potentiometric or solid state electrolyte (YSZ) oxygen sensor [22], [23]. When gas contact with the working electrode, oxidation occurs on it. Short circuit connects the working and counter electrodes which allow ion flow [25].

Capacitance based gas sensors measure the change in dielectric constant of films as a function of gas concentration [22].

Non-dispersive infrared gas sensors measure decrease in transmitted infrared light. Interaction between the gas molecules and infrared light results in adsorption of the light at particular wavelength and vibration of gas molecules. The ratio of transmitted radiation energy to the incident energy differs with the gas concentration [25].

Acoustic wave gas sensors also known as sound based composed of piezoelectric material either in thin film or in bulk to introduce acoustic waves to transducer [22].

1.5.3 Why are we detecting CO_2?

CO_2 is an inert gas which is present at concentrations (as of September 2019) of 408.55 ppm in Earth atmosphere [26]. It is used in fire extinguishers, carbonated drinks, manufacturing of casting molds and hardness of metals, as raw material in urea and methanol production, in oil extraction, an additive to oxygen for medical use, a propellant in aerosol cans, as dry ice and essential part of the process for lasers and refrigerators [27].

CO_2 is also an important greenhouse gas. Earth's land and ocean surfaces are warmed by sunlight and radiate thermal infra-red energy (heat). CO_2 absorbs this energy then

gradually release to surrounding. Although it absorbs less energy per molecule then methane or nitrous oxide, it is more abundant and stays longer in the atmosphere. Because of these reasons, increasing atmospheric CO_2 concentration causes two-thirds of the total energy imbalance that causing global warming as shown in Figure 1-10 [28].

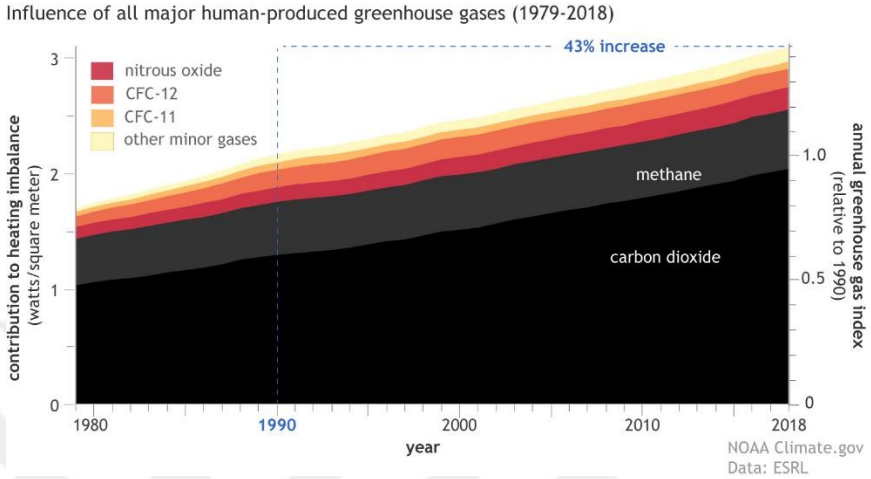

Figure 1-10 : Heating imbalance caused by human-produced greenhouse gases [22]

Moreover, CO_2 gas dissolves in oceans and forms carbonic acid reacting with water. Carbonic acid causes decrease the pH of the oceans. Since Industrial Revolution pH of the ocean change through 8.21 to 8.10. This situation is called ocean acidification and intrude the ability of the marine life extracting calcium from water which they use it building their shells and skeletons [28].

CO_2 gas can have negative effect on human health. Table 1-2, which is taken from occupational health and safety website in Canada, displays symptoms of exposure to CO_2 [29].

Table 1-2 : The health effect of exposure to CO_2 gas [23]

CO_2 Concentration and Exposure time	**Effect on health (symptoms)**
0.035%	Approximate atmospheric concentration, no noticeable effect.
3.3–5.4% for 15 mins	Increased depth of breathing
7.5% for 15 mins	Feeling of an inability to breathe, increased pulse rate, headache, dizziness, sweating, restlessness, disorientation, and visual distortion.

3%, for over 15 hours	Decreased night vision, color sensitivity
10%, 1.5 mins	Eye flickering, increased muscle activity, twitching
10+%	Difficulty in breathing, impaired hearing, nausea, vomiting, a strangling sensation, sweating, after 15 minutes a loss of consciousness.
30%	Unconsciousness, convulsions. Several deaths attributed to CO_2 at concentrations of more than 20%

CO_2 gas also important for the carbon cycle. Carbon cycle describes the process that carbon atoms travel from the atmosphere to Earth then again back to atmosphere. On Earth, carbon atoms can be found in rocks and sediments, oceans, living organisms and atmosphere. On release part when organisms die, volcanoes erupt, with fires. Moreover, humans contribute the cycle burning fossil fuels [30].

1.5.4 Gas Sensing Mechanism

Determining sensing mechanism of metal oxides is important for designing device and developing material properties according to results. Although exact mechanism is still questionable, trapping of electrons at adsorbed molecules and band banding caused by charged molecules lead to changes in conductivity during gas transition [31].

Band Theory

Semiconductor material properties can be understood as looking its electronic structure difference from the metals. Usually, the electronic structure of these solids is described in terms of energy bands produced by the atomic orbitals of the individual atoms. Because of the vast number of orbitals, the difference in energy within a given energy band between neighboring molecular orbitals is so minimal that the band can be effectively considered a continuum of energy levels. The energy bands of interest are the highest occupied (called the valence band) and the lowest (called the conduction) unoccupied. The properties of the material are determined by the energy distance (the band distance) between those bands (i.e., the difference in energy between the upper edge of the valence band and the lower edge of the conductive band). The band gap is not large for semiconductors, so electrons can be transferred into the conduction band [32].

Electrons may be thermally or photochemically stimulated to the conduction band. However, there is another process inside a semiconductor for producing charge carriers (i.e., electrons or holes), called doping. Doping implies adding another element to the semiconductor [32].

Undoped semiconductors are called as intrinsic semiconductors. Doped semiconductors in which the dominant charging carriers are electrons are referred to as the n type, whereas those in which holes are the predominant charging carriers are referred to as the p-type as shown in Figure 1-11 [32].

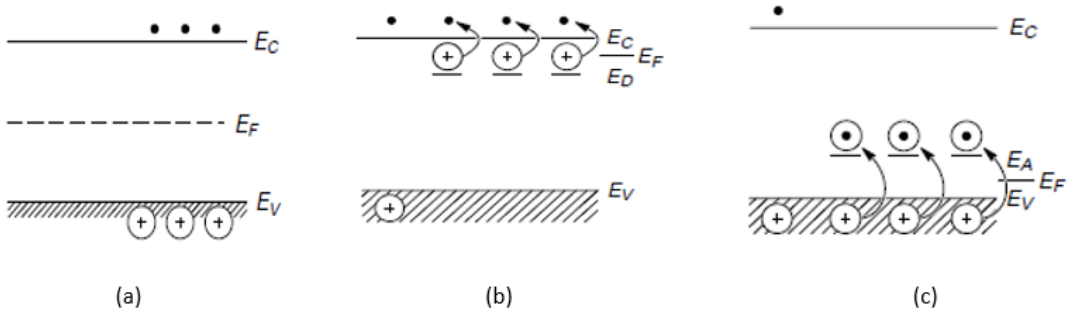

Figure 1-11 : Schematic diagram of energy levels of (a) intrinsic semiconductor (b) n-type semiconductor and (c) p-type semiconductor [26]

Fermi level is another significant term in addressing solid state materials. It is known as the energy level at which an electron's probability of occupation is 1⁄2; for example, the Fermi level lies at the midpoint of the band gap for an intrinsic semiconductor. Doping changes the distribution of electrons within the solid, and thus affects Fermi level [32].

Band Bending

The energy band edges of semiconductors can shift due to the charge transfer between electrical field of the semiconductor and the metal in the space charge region. This case is called as band bending [33].

Negatively charged layer in the metal creates repulsion upon the electrons of the semiconductor that causes potential energy rising and upward bend bending. The opposite case causes downward bend bending [33].

The gas sensor and electrochemistry fields exploit the band bending concept as understanding photo-process and controlling the efficiency in charge transfer and creating electronic or chemical devices with the semiconductors. For research, several

different methods are used like photoelectron spectroscopy (PS), photoluminescence spectroscopy, scanning probe spectroscopy, Raman spectroscopy, etc. [28].

General Mechanism

One the important aspect of gas sensors is the knowing mechanism and through this information, designing and fabricating the sensor. Although exact gas sensing mechanism of metal oxides is still controversial, it is based on the resistance or conductivity change occurs due to the electron trapping on the absorbed molecule and bend bending of the sensing material [34].

Oxygen species catch the negative charge which causes an upward band bending and, in this manner, conductivity decreases. When O_2 particles are adsorbed on the surface of metal oxides, electrons are discharged from the conduction band E_C and electrons are trapped at the surface. This will lead a band bending and an electron depletion region or another name space-charge layer. Reaction with reducing gases causes opposite effect and conduction increases due to downward band bending which is caused from replacement of adsorbed oxygen [34].

Density function theory (DFT) calculations may be used to understand the CO_2 sensing mechanism. According to Wang.et al[35], measurement was done with optimized LaMnO3 (0 1 0) surface. During the adsorption process, different modes were observed and most suitable one was decided through the distance between adsorbed CO_2 molecules and bonding sites on the surface, bonding angle of adsorbed CO_2, charge-transfer, and adsorptive energies. Figure 1-12 shows the most logical and suitable model [35].

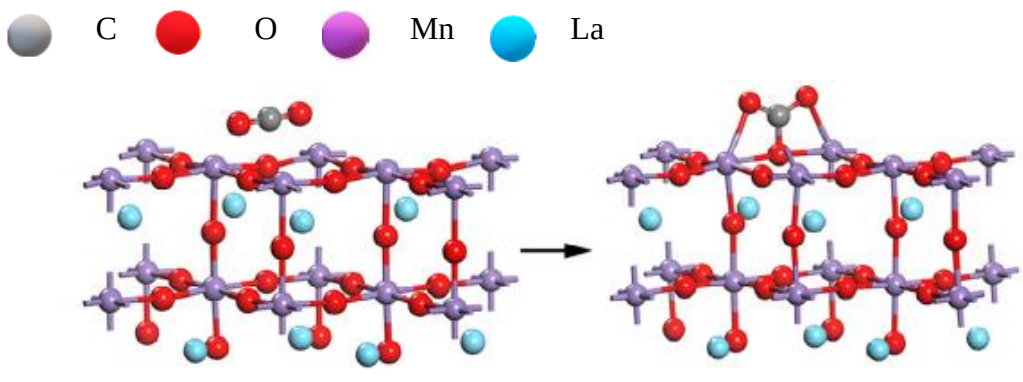

(I)

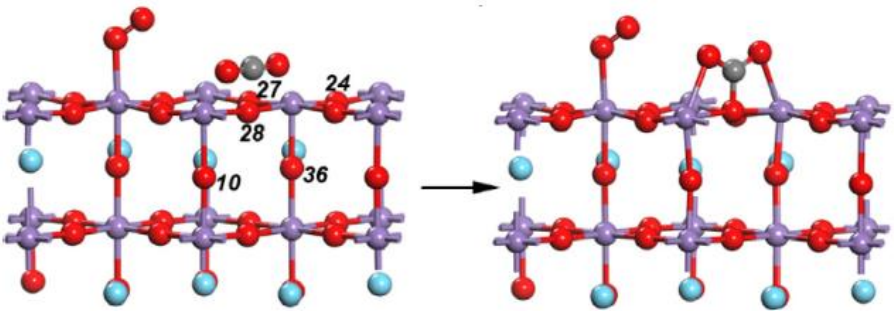

(II)

Figure 1-12 : DFT model CO_2 gas passing parallel to surface (I) clean surface (II) O_2 bonded surface[29]

One oxygen atom of CO_2 was bonded with two manganese atoms and one oxygen atoms on the surface showed the shortest bond, the minimum bond angle and max adsorptive energy. CO_2 acted as donor and increasing resistance pointed the reduction in the positively charged holes of p-type semiconductor [35].

When compared (I) and (II), pre-bonded O_2 decrease the adsorption of CO_2 molecule however CO_2 molecules lost more electron on the pre-adsorbed O_2 surface due to the transferred electrons of O atom near the CO_2 molecule [35].

1.5.5 Device Structure and Fabrication Methods

Gas sensors conventionally made of three main parts as seen in Figure 1-13. Metal oxide thin film on substrate which will react with the gas and show change in resistance. Electrodes which measure the resistance of the sensing film and external heater for reaching optimum working environment [31].

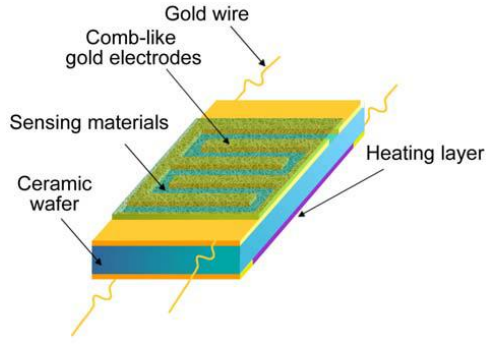

Figure 1-13 : Device structure based on ceramic substrate [31]

This device is called as interdigitated electrode. As seen in Figure 1-14, IDEs based on two electrodes which contain individual digits that were arranged like comb to form micro-size gaps between each electrode. Comb-like structure helps to produce simple, easy to use, and inexpensive sensor. When AC or DC voltage was applied to electrodes, the electric field will occur between them in this way, resistance or current becomes measurable [36].

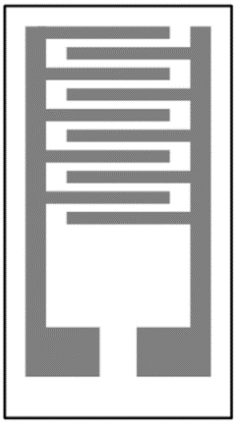

Figure 1-14 : Standard IDE

IDEs conventionally fabricated using photolithography technique. Also, electrode material is important for the sensing ability so much research was conducted about this. Novel metals like palladium, gold, silver, or platinum were preferred due to their good stability. Platinum is the most stable one among them and shows little degradation but is very expensive. Silver is the cheapest one and stable in air but with the humidity, it migrates over surface of the resistors. Gold has high conductivity and reliability but can diffuse in silicon like substrate at low temperatures [36].

For sensor fabrication, several methods like spin coating, electrophoretic deposition (EPD), chemical vapor deposition (CVD), spray pyrolysis, screen printing, drop coating and physical vapor deposition.

Spin Coating

Spin coating is a method that use speed and rotation to create a uniform film and one of the most common methods that used in industry. General theory behind is the centripetal force, which caused from high rotation speed, conjoined with surface tension of the solution [37]. Figure 1-15 shows the coating steps.

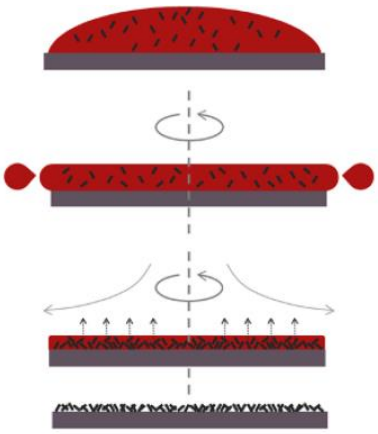

Figure 1-15 : Spin coating steps (a) substrate coated with ink (b) rotated substrate (c) solvent started to evaporate (d) fully dried film with molecules on it [37]

There are several parameters that should carefully decide to get uniform and thin or thick film: rotation speed, drying time and wetting effect of the solvent and ink, spin time and dispense technique (static or dynamic). Spin speed will directly affect the thickness of the film and the quality because concentration of the ink has also effect on thickness. Solvent selection will affect the spin time, drying time and quality because of different boiling points and vapor pressures. For most solvent like acetone, ethanol, toluene, etc., 30 s will be sufficient but for solvents that have high boiling point or lower vapor pressure, drying will take longer time. Moreover, dispense technique is another parameter. In dynamic dispense, solution will be dropped after rotation started but in static dispense, first solution is dropped then rotation will start. Generally, for more viscous solutions static dispense technique is used [37].

Electrophoretic Deposition (EPD)

The electrophoretic deposition method is based on the migration and eventual deposition of charged particles in a stable suspension, caused by applying an electric field between two electrodes [38].

In EPD, solvent evaporation is followed by the electrically assisted formation of a cohesive layer of particles. Therefore, deposit yield and molecule pressing in electrophoresis not just rely upon the steadiness and the solids substance of the suspension, yet on the accumulation and arrangement of the particles on the surface of the electrode. Surface chemistry, the conduct of the surface–fluid interfaces under an electric field, and the improvement of particle-particle and particle- substrate systems

during aggregation will affect the obtaining homogeneous and solid film [38]. Figure 1-16 schematically show the EPD process.

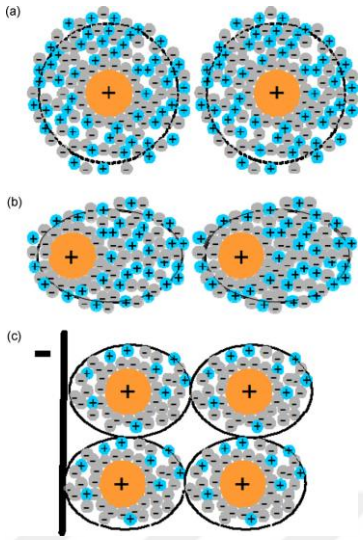

Figure 1-16 : Scheme of (a) Electrostatically dispersed particles (b) deformed double layer (c) concentration change in the electrode boundary.[31]

Drop Casting

Drop casting is an easy and cheap deposition method for small areas. In principle, controlled size droplets are released over a substrate, wet the substrate, and allowed the dry under controlled conditions (pressure and temperature). Figure 1-17 shows the drop casting deposition [39].

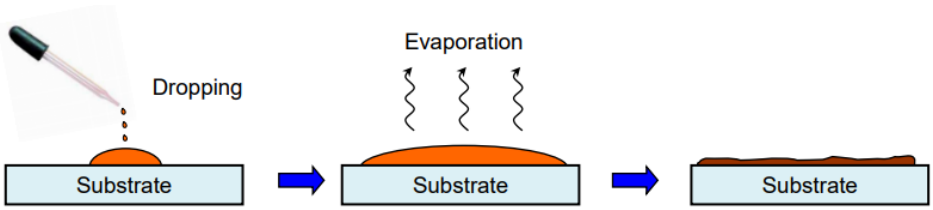

Figure 1-17 : Drop casting deposition [32]

Screen Printing

Commercially available metal oxide gas sensors are generally produced by screen printing method in industry as seen in Figure 1-18. Ink is essential component for screen printing. It contains the viscous material to be deposited on a substrate layer.

Then the ink is pushed through a porous layer to create aimed layout. Finally, heat is applied, and solid material stay on targeted area [33].

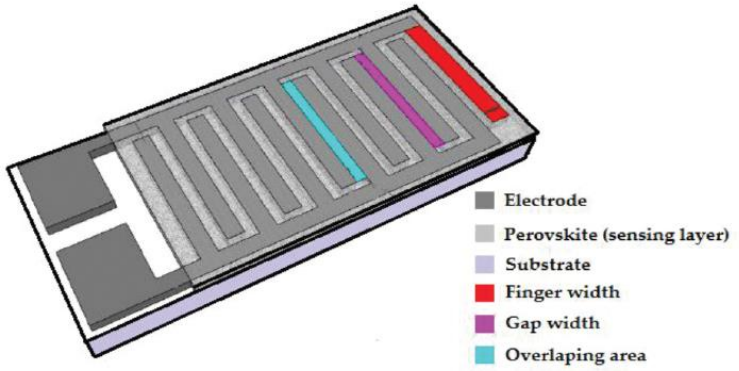

Figure 1-18 : Screen printed gas sensor[33]

1.5.6 Factors Influencing the Sensors Performance

Different properties were affected by the synthesis method, calcination time and A-B site substituents.

Metal Doping

Doping is a widely used technique at sensing area. Partial or total substitution of A and/or B site cations will make difference in catalytic activity and modify the electrical resistance of metal oxide because it creates oxygen vacancies and different oxidation states, affects the mobility and stability of oxygen lattice and formation of structural defects [8].

Increased surface conductivity can be explained with the mechanism; gases are absorbed on dopant's surface then migrates the oxide's surface to react with oxygen species. Another role of doping is better the gas sensing ability to create electron transfer from n-type material to p-type material, which is called as p-n junction. Depletion barrier height raised with p-n junction. If highly sensitive nanostructures were doped, sensitivity will increased dramatically [31].

Humidity

Environmental humidity is another significant factor that affecting the metal oxide gas sensors performances. Although water vapor sensing mechanism is different than

pollution gases and not donate electron to sensing layer, it has lowering effect on the performance of metal oxides. Water molecule reaction with surface oxygen reduces the baseline resistance of gas sensor and causes decrease in sensitivity. Secondly, water vapor molecules that bound the active site prevent chemisorption of oxygen species. Moreover, long exposures humid environment causes stable chemisorbed OH^- and result in lessen sensitivity but high temperatures like 400-450 ^oC remove the OH^- ion and lead the recovery [34].

Temperature

Temperature has effect on gas sensing because it influences kinetics and chemisorption [34]. Temperature-dependent response curve is typical for the most gas sensor. First, response increases with the rising temperature and reach the optimum then decreases rapidly [40]. This behavior can be explained as at the low temperatures, gas molecules do not have sufficient thermal energy to react with the adsorbed oxygen species. Conduction band electrons are drawn by absorbed oxygen and potential barrier to charge transport is occurred. At high temperature, energy is enough for the overcoming the potential barrier and sensing reaction is observed due to increased electron concentration. If chemical reaction activation energy is high, sensing reaction at low temperatures is restricted by chemical reaction speed, at higher temperatures is restricted by speed of diffusion of gas molecules. At different intermediate temperatures diffusion rate and chemical reaction speed become equal and sensor response reaches its maximum [41].

1.5.7 Gas Sensor Characteristic of Metal Oxides

Sensitivity

Chemiresistive metal oxide gas sensors' responses are generally defined in terms of conductivity or resistivity. According to this, sensitivity is the response of a gas sensor per unit change in the gas concentration [22]. Sensitivity (S) is showed as R_a/R_g for reducing gases and R_g/R_a for oxidizing gases where R_a is resistance of the reference gas and R_g is the resistance of the targeted gas containing reference gas in it [34].

Stability

Stability is a sensor's ability to produce repeatable results over a given period. This involves maintaining sensitivity, selectivity, response and recovery time [42]. Practical

use of a device is highly dependent to stability and reproducibility. Ideal gas sensor should operate 2-3 years (17,000-26,000 h). In account to metal oxide gas sensors, stability can be affected from morphological changes (crystal size, number and distribution of grains) of sensing material, new phase occurrence due to interaction with the gas and reaction with the substrate [43].

Selectivity

Selectivity determines if the sensor give response only a particle molecule or group of analyte in the mixture or environment [42]. Generally sensing materials respond more than one gas compound to overcome this problem, wide range operating temperatures can be tried to detect different thermal energies for the surface reactions or surface modification can made or highly selective physical and chemical filters can used to prevent permeation of other gases than targeted one/s [44].

Response and Recovery Time

The time required for the determination of changing starting from zero to certain concentration is called response time [42].

The time required for sensor to turn 90% of its initial signal value as target gas is removed from the system is called recovery time [22].

In real life, fast response and recovery time is essential for the detection of explosive, toxic and dangerous gases. When sensor materials are adequately disperse, quick gas diffusion and fast reaction between the oxygen anions and analyte gas can obtain to achieve aimed property [45].

Detection Limit

Under given conditions, the minimum concentration that can be detected by the sensor is referred as detection limit [42].

Dynamic Range

Dynamic range is the range of concentration between the limit of detection and the maximum limiting concentration [22].

Accuracy and Resolution

Accuracy is a capacity to produce results similar to the true value of the quantity measured. Absolute and relative errors are used to determine the accuracy percentage [46].

Resolution is the lowest difference in concentration which the sensor can differentiate [46].

1.6 Material Characterization Techniques

1.6.1 X-Ray Diffraction Spectroscopy

X-rays are type of electromagnetic radiation that have high energies and short wavelength. When the x-ray beams collide with solid material, part of the beam scattered in all directions and their intensities are determines by periodicity of atom planes in the solid. Braggs equation explains the geometry mathematically [47].

$$2d_{hkl} \sin \theta = n\lambda \quad \textbf{(1.3)}$$

n is order of reflection (n=1,2, 3..), d_{hkl} is the magnitude of the distance between the two parallel and adjacent planes as a function of Miller indices (h,k and l) , θ is the incident angle and λ is the wavelength of the x-ray beam (Figure 1-19) [47].

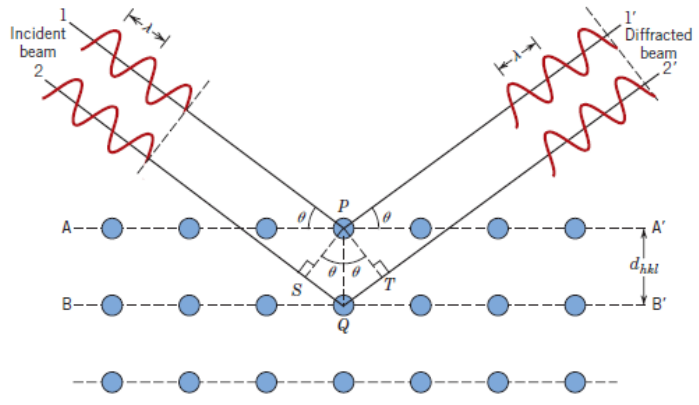

Figure 1-19 : Bragg equation construction for X-ray diffraction [42]

The main idea behind it is the match the positions and the intensities of the peaks that observed with the calculated standard diffraction pattern to identify the unknown material [48].

In powder diffraction method, Debye-Scherrer method is applied. Monochromatic X-ray beam interacts with the specimen which contains enough particle that allows diffraction from all possible diffracting planes like in Figure 1-20 [47].

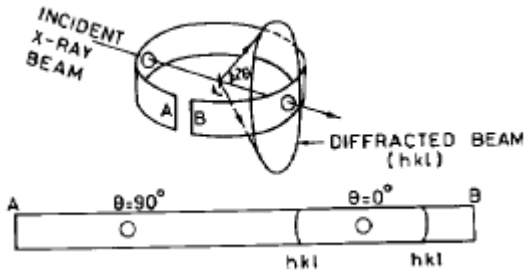

Figure 1-20 : Schematic diagram of Debye-Scherrer method [41]

The peak positions supply crystal structure and lattice parameters for the powder specimen. These information use for the determination of phase diagram boundaries, thermal expansion coefficient, position and distribution of the atoms in crystal, density and composition [47].

1.6.2 X-Ray Fluorescence Spectroscopy

X-rays, comes from X-ray tube or radioactive source, irritate the sample. The elements in the sample are excited by adsorption and emit their own characteristic fluorescence and this method is called X-ray fluorescence (XRF) or X-ray emission [49].

XRF measures intensities of X-rays emitted from specimen and it varies with the amount of atom and the characteristic lines defines atoms in the sample. The emission occurs when a vacancy is filled with outer orbit electron (transition). The energy is equal to difference between the energy levels (Figure 1-21) [50].

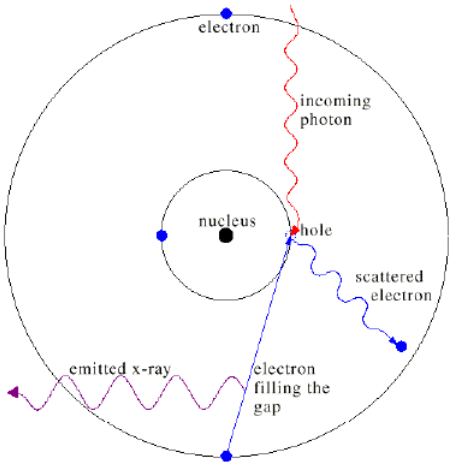

Figure 1-21 : Schematic representation of X-ray fluorescence [50]

For XRF spectroscopy, principal is same, but instrumentation can show difference as function of wavelength or energy. Moreover, one of the important aspects is the way the inner vacancy is created. Bombarding the sample with high energy X-ray which leads photon adsorption or high energy electrons and protons which creates Coulomb interactions [50].

1.6.3 Scanning Electron Microscopy

Scanning electron microscope is used for analysis of microstructure morphology and chemical composition characterization. SEM images were obtained from a signal that caused from interaction between the electron beam and the specimen. These interactions were mainly separated into two and called as elastic and inelastic interactions. Specimen atomic nucleus or outer shell electrons that have similar energies cause deflection of incident electron and called as elastic scattering. When incident beam loses its energy through the interaction this called inelastic scattering [51]. Figure 1-22 shows the signals caused from electron-specimen interaction.

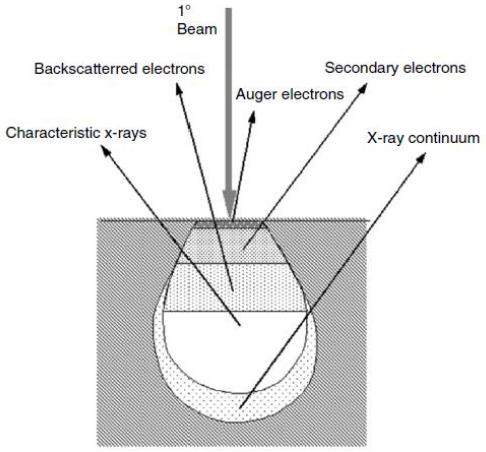

Figure 1-22 : Illustration of SEM signals and regions that they occurred [46]

Characteristic X-rays are created when inner shell electron is removed, and outer shell electron falls into inner shell to balance the charge. These rays are used to and identify the composition and abundance of the elements in the sample [52].

Backscattered electrons (BSE) is elastically scattered through more than 90 degree and generally used with characteristic X-ray in analytical SEM because the signal of BSE is strongly related to atomic number (Z) of specimen [52].

Secondary electrons are generated as ionization product. When the primary beam hits the surface of specimen, some loosely bound electrons can be emitted. They have low energies and used for high resolution images of the surface [51], [52].

Chapter 2:**EXPERIMENT**

2.1 Material Preparation

2.1.1 $LaTiO_3$ based powder preparation

All reagents used in this work were of analytical grade and used without further purification. $LaTi_{(1-x)}B_xO_3$ (B: Co or Ni or Fe) and $La_{(1-x)}A_xTiO_3$ (A: Sr or Ca) samples were synthesized by the sol-gel method described as follows. Firstly, TIP (isp) was added to methanol. After no precipitation is observed metal salts were added in the stoichiometric proportions corresponding to different values of x. Later, citric acid was added to the solution and stirred until a homogenous solution was obtained, then heated up to 60 ^oC with continuous stirring. Finally, ethylene glycol was put in clear solution and stirred up to gel consistency. The obtained gel was charred on a heating mantle at 350-400 ^oC, and then calcinated at 900 ^oC for 2 hours (5 ^oC/min). The flowsheet for synthesis of LTO powder can be seen in Figure 2-1.

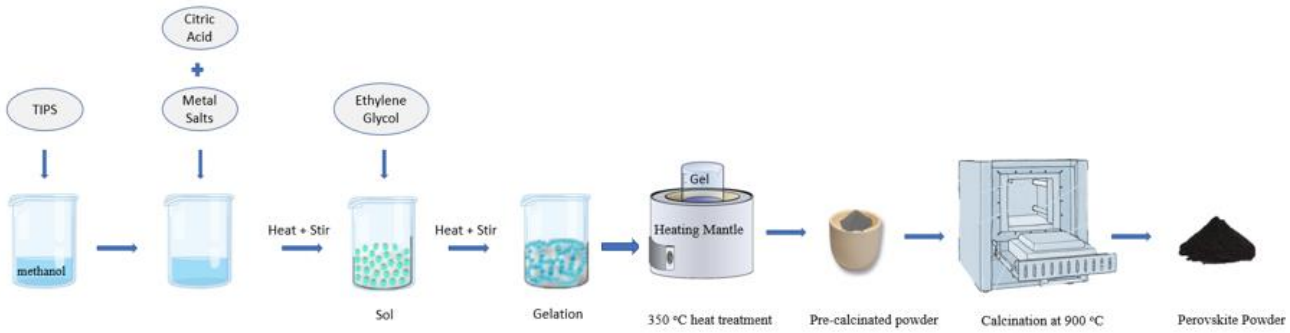

Figure 2-1 : Synthesis process of LTO powders

2.1.2 Ag doped LaTiO3 based powder preparation

$LaTiO_3$ based powder, which was prepared according to 2.1.1, was mixed with $AgNO_3$ in the weight ratio 2:1 and crushed manually for at least 15 min. Then the mixture was calcinated at 900 ^oC for 2 hours (5 ^oC/min).

2.1.3 $LaMnO_3$ based powder preparation

All reagents used in this work were of analytical grade and used without further purification. $LaMn_{(1-x)}B_xO_3$ (B: Co or Ni or Fe) and $La_{(1-x)}A_xMnO_3$ (A: Ca) samples were synthesized by the sol-gel method described as follows. Firstly, metal salts were solved in distilled water by the stoichiometric proportions corresponding to different values of x, the solution was heated to 60 °C. After addition of citric acid, the temperature of the solution was raised to 80 °C and ethylene glycol was added and stirred until gel formation was observed. The obtained gel was charred at 350°C (5 °C/min), and then calcinated at 700 °C for 4 to 6 hours (5 °C/min). The flowsheet for the synthesis of LMO powder can be seen in Figure 2-2.

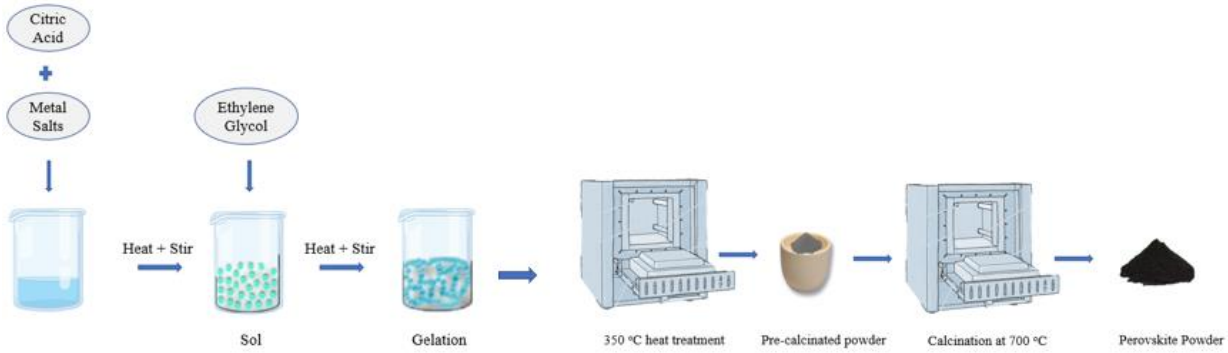

Figure 2-2 : Synthesis process of LMO powder

2.1.4 Film Preparation

For obtaining uniform and adequate film, powders were dispersed in different solvents such as ethanol, methanol, acetonitrile, or acetone. After the proper solvent was chosen, various powder: solvent ratios were tested.

Drop casting, EPD, and spin coating methods were tested. Spin coated films resulted in more uniform thin film. After the method was chose, different layer numbers were tried. As a typical procedure, 60 mg perovskite powder was dispersed in 2.5 mL ethanol and treated in ultrasonic bath for 30 to 60 min. The dispersion was spin coated on interdigitated electrodes (Metrohm DropSens DRP-IDEAU200) at a speed of 2000 rpm for 30 s. The spin coating procedure was repeated ten times to obtain smooth and homogenous films with 10 layers. Images of the films can be seen in Figure 2-3.

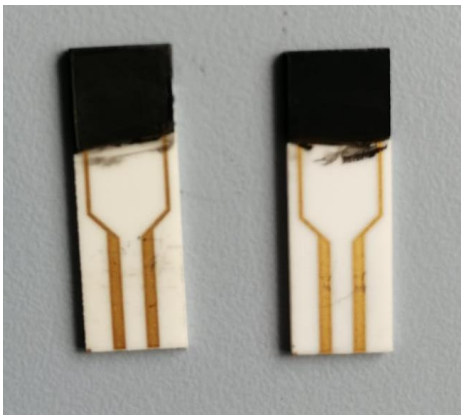

Figure 2-3 : Spin coated interdigitated electrodes for gas sensing

2.1.5 Characterization of samples

The crystalline structures of the prepared perovskite oxides were examined by X-ray diffractometer with Cu Kα radiation (XRD, Bruker D2 Phaser) in the 2θ range of 20^{o} to 80^{o} and the crystallite size was determined with Scherrer evaluation calculations based on full width at half maximum of XRD peak by Diffrac.EVA program, elemental composition was determined with X-ray fluorescence spectrometer (XRF, Bruker Tiger S8), and the surface morphology was examined with the field emission scanning electron microscopy (FE-SEM, Zeiss Ultra Plus) using accelerating voltage of 2 kV.

2.2 Resistivity Measurement

For resistivity measurement, homemade gas sensing chamber was designed and shown in Figure 2-4.

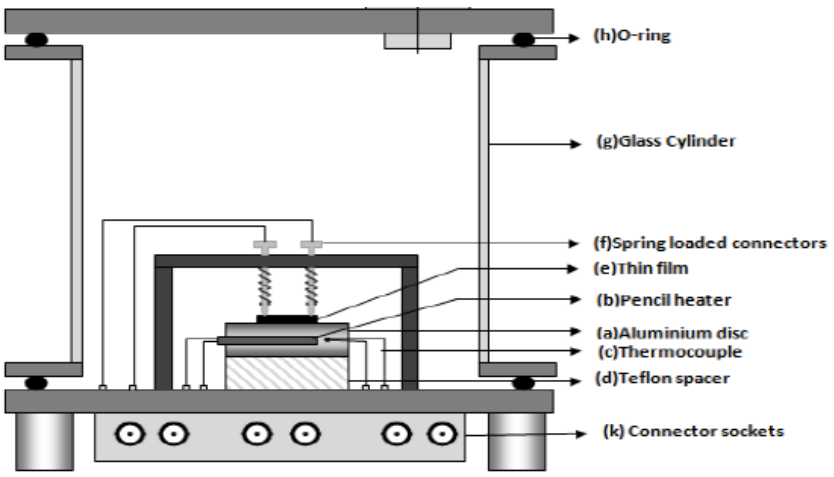

Figure 2-4 : Gas sensing chamber and its components [53]

Components of the experimental setup was visualized in Figure 2-5. CO_2 gas and dry air were connected to homemade chamber via flowmeter and mass flow controller (Alicat Scientific) to adjust concentrations of the gases. Gas outlet pipe was put in the water bottle to see and observe the gas flow. Then, thermocouple was connected to temperature controller and Keithley Bench Sourcemeter (B2901A) was connected the homemade measurement chamber. Measured resistance values were read and recorded with the computer. During the experiment constant dc voltage of 10 V was applied.

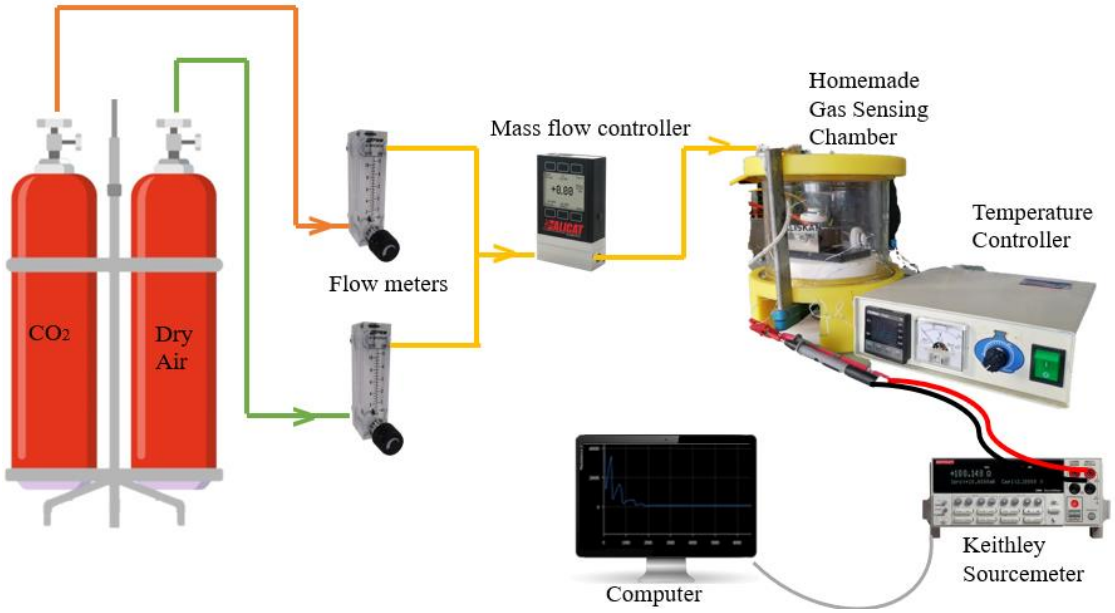

Figure 2-5 : Homemade setup for CO_2 gas sensing measurements

After the powder coated electrode was placed in homemade chamber and chamber was sealed tightly, dry air was opened at room temperature. For 30 minute, only dry air flowed through system with 2L/min or 10L/min for the stabilization of the medium. Then the system was heated up until it reached low resistivity at high temperature like 250-300 ^oC with 50 ^oC intervals. After the stability is obtained at aimed temperature, CO_2 gas is flow with different time intervals without interrupting the dry air flow. The concentrations of CO_2 in the gas mixture was controlled with a mass flow controller. Finally, resistivity was monitored under the flow of gas mixture.

Chapter 3:**RESULTS AND DISCUSSION**

3.1.1 $LaTi_{(1-x)}Ni_xO_3$ and $LaMn_{(1-x)}Ni_xO_3$ (x = 0, 0.2, 0.4, 0.6, 0.8 and 1)

X-ray diffraction diagrams of nickel doped LTO phases and LaNiO3 (LNO) at 20%, 40%, 60% and 80% are shown in Figure 3-1. The sharpness of the diffraction peaks indicated that a crystalline and pure structure was obtained. According to XRD diagrams, the La_2O_3 impurity phase was observed in the 20% nickel doped sample. The samples, which had dopant $x \geq 0.4$, showed no impurities. When the diagrams were examined, the increase in the amount of Ni dopant caused to change in the crystal structure. LTO samples with 20%, 40%, 60% Ni doped exhibited cubic structure (PDF 04-006-0088), LTO-Ni-0.8 and LNO were crystallized in rhombohedral structure. With this change, peak positions shifted to higher 2Θ values towards the $LaNiO_3$ structure (PDF 00-033-0711). By changing the amount of additive, the amount of Ni element which was replacing Ti element had changed and the crystallite size had adjusted accordingly. The crystallite size was expected to increase, and the surface area was expected to decrease moving toward the $LaNiO_3$ structure (Table 3.1). When the results of X-ray fluorescence spectroscopy were examined, it was seen that almost all targeted nickel amount could be added to the structure (Table 3-1).

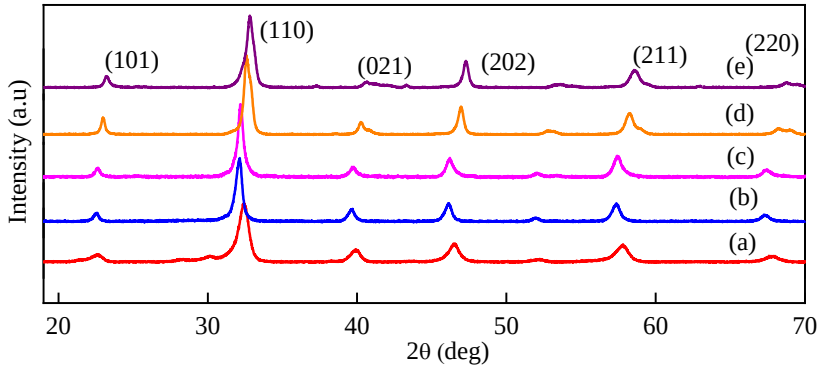

Figure 3-1: X-ray diffraction diagrams of LTO-Ni-x powders (a) $LaTi_{0.8}Ni_{0.2}O_3$, (b) $LaTi_{0.6}Ni_{0.4}O_3$, (c) $LaTi_{0.4}Ni_{0.6}O_3$, (d) $LaTi_{0.2}Ni_{0.8}O_3$, and (e) $LaNiO_3$

Table 3-1 : X-ray characterization of LTO-Ni-x powders

Sample Name	X-Ray Fluorescence Spectroscopy			X-Ray Diffraction Spectroscopy	
	La	Ti	Ni	Phase Structure	Crystalline Size (nm)
LTO-Ni-0.2	1	0.86	0.26	Cubic	17
LTO-Ni-0.4	1	0.5	0.42	Cubic	18
LTO-Ni-0.6	1	0.35	0.62	Cubic	18
LTO-Ni-0.8	1	0.17	0.81	Rhombohedral	24
LNO	1		1.05	Rhombohedral	26

X-ray diffraction diagrams of nickel doped LMO phases at 20%, 40%, 60% and 80% are shown in Figure 3-2. The sharpness of the diffraction peaks indicated that a crystalline and pure structure were obtained. According to XRD diagrams, La_2O_3 phase was not observed in $x \leq 0.6$ nickel doped sample. However, in 80% doped sample, La_2O_3 phase is observed. This phase disappeared at 900 ^oC but calcination temperature was kept as 700 ^oC in order to prevent the increase in the crystallite size. When the diagrams were examined, the increase in the amount of Ni dopant caused the change in the crystal structure. LMO-Ni-0.2 and LMO-Ni-0.4 samples exhibited cubic structure (JCPDS No.01-083-4423), LTO-Ni-0.6 and LTO-Ni-0.8 exhibited rhombohedral structure (JCPDS No.00-055-0695). With this change, peak positions shifted to higher 2Θ values towards the $LaNiO_3$ structure (PDF 00-033-0711). By changing the amount of additive, the amount of Ni element which was replacing Mn element had changed and the crystal size had adjusted accordingly. The crystal size decreased due to smaller radius of Ni ion compared to radius of Mn ion. (Table 3.2). When the results of X-ray fluorescence spectroscopy were examined, it was seen that almost all targeted nickel amount could be added to the structure (Table 3-2).

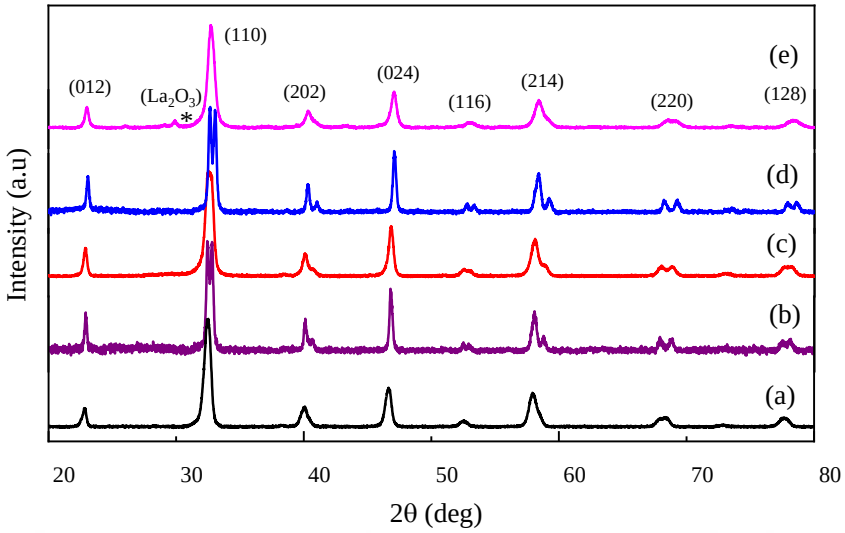

Figure 3-2 : X-ray diffraction diagrams of LMO-Ni-x powders (a) $LaMnO_3$, (b) $LaMn_{0.8}Ni_{0.2}O_3$, (c) $LaMn_{0.6}Ni_{0.4}O_3$, (d) $LaMn_{0.4}Ni_{0.6}O_3$, and (e) $LaMn_{0.2}Ni_{0.8}O_3$

Table 3-2 : X-ray characterization of LMO-Ni-x powders

Sample Name	**X-Ray Fluorescence Spectroscopy**			**X-Ray Diffraction Spectroscopy**	
	La	**Mn**	**Ni**	**Phase Structure**	**Crystalline Size (nm)**
LMO-Ni-0.2	1	0.75	0.21	Cubic	18
LMO-Ni-0.4	1	0.58	0.44	Cubic	23
LMO-Ni-0.6	1	0.39	0.63	Rhombohedral	20
LMO-Ni-0.8	1	0.2	0.86	Rhombohedral	23

The SEM images showing the surface morphology of the samples are given in Figure 3-3 and Figure 3-4. These SEM images show that sample have porous structure comprised of perovskite nanoparticles.

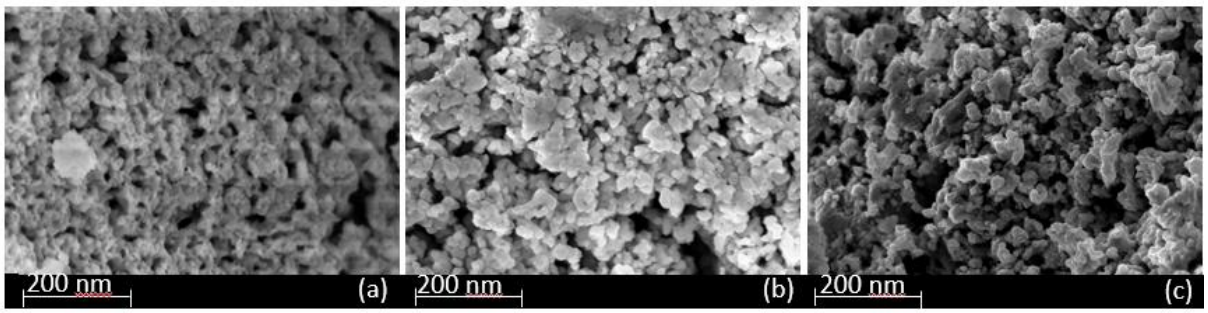

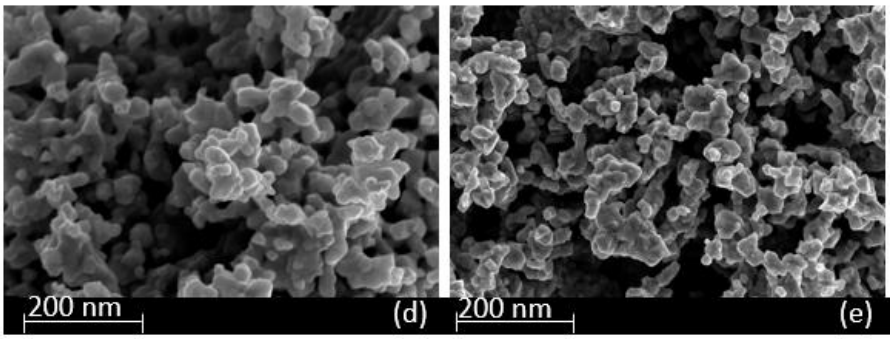

Figure 3-3 : SEM images of LTO-Ni-x powders at 200 nm scale x: (a) 0.2, (b) 0.4, (c) 0.6, (d) 0.8, and (e) 1

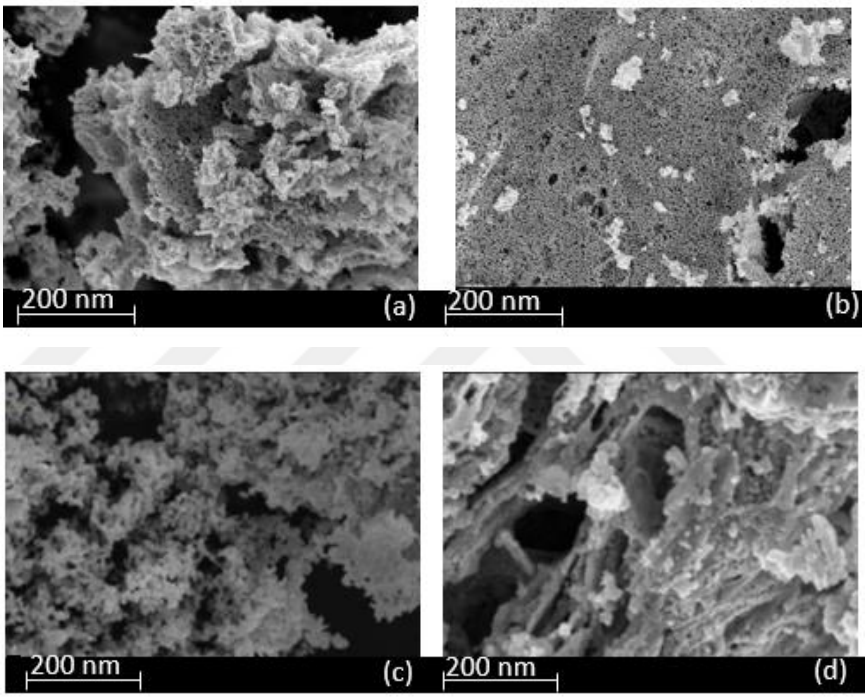

Figure 3-4 : SEM images of LMO-Ni-x powders at 200 nm scale x : (a) 0.2, (b) 0.4, (c) 0.6, and (d) 0.8

3.1.2 $LaTi_{(1-x)}Co_xO_3$ and $LaMn_{(1-x)}Co_xO_3$ (x = 0, 0.2, 0.4, 0.6, 0.8, and 1)

X-ray diffraction diagrams of cobalt doped LTO phases and $LaCoO_3$ (LCO) at 20%, 40%, 60% and 80% were shown in Figure 3-5. The sharpness of the diffraction peaks indicated that a crystalline and pure structure was obtained. According to XRD diagrams, the La_2O_3 phase was observed in the 20% cobalt doped sample. The samples, which had dopant of $x \geq 0.4$, showed no impurities. When the diagrams were examined, the increase in the amount of cobalt caused to the crystal structure to be changed. LTO samples with 20%, 40%, 60% Co doped were exhibited cubic structure (PDF 04-006-0090), LTO-Co-0.8 and LCO were crystallized in rhombohedral structure (PDF 00-025-1060). With this change,

peak positions shifted to higher 2Θ values towards the $LaCoO_3$ structure. By changing the amount of additive, the amount of Co element which was replacing Ti element had changed and the crystal size has changed accordingly. The crystal size was expected to increase as moved toward $LaCoO_3$ structure (Table 3-3). When the results of X-ray fluorescence spectroscopy were examined, it was seen that almost all targeted cobalt amount could be added to the structure (Table 3-3).

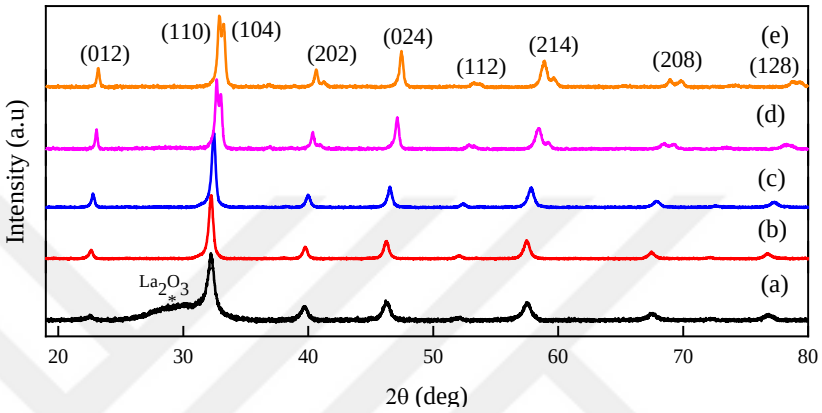

Figure 3-5 : X-ray diffraction diagrams of LTO-Co-x powders (a) $LaTi_{0.8}Co_{0.2}O_3$, (b) $LaTi_{0.6}Co_{0.4}O_3$, (c) $LaTi_{0.4}Co_{0.6}O_3$, (d) $LaTi_{0.2}Co_{0.8}O_3$, and (e) $LaCoO_3$

Table 3-3 : X-ray characterization of LTO-Co-x powders

Sample Name	X-Ray Fluorescence Spectroscopy			X-Ray Diffraction Spectroscopy	
	La	Ti	Co	Phase Structure	Crystalline Size (nm)
LTO-Co-0.2	1	0.82	0.20	Cubic	17
LTO-Co-0.4	1	0.59	0.40	Cubic	21
LTO-Co-0.6	1	0.42	0.58	Cubic	24
LTO-Co-0.8	1	0.22	0.88	Rhombohedral	32
LCO	1		1.15	Rhombohedral	50

X-ray diffraction diagrams of cobalt doped LTO phases and $LaCoO_3$ (LCO) at 20%, 40%, 60% and 80% were shown in Figure 3-6. No impurities were seen in the samples. When the diagrams were examined, the increase in the amount of cobalt caused to the crystal structure to be changed. LMO-Co-0.2 and LMO-Co-0.4 exhibited cubic structure (JCPDS No.04-005-7818), LMO-Co-0.8 and LTO-Co-0.8 exhibited rhombohedral structure (JCPDS No.04-012-5615). With this change, peak positions shifted to higher 2Θ values towards the LaCoO3 structure. When the results of X-ray fluorescence spectroscopy were

examined, it was seen that experimental ratios were little bit higher than targeted cobalt amount, but these values were tolerable. (Table 3-4).

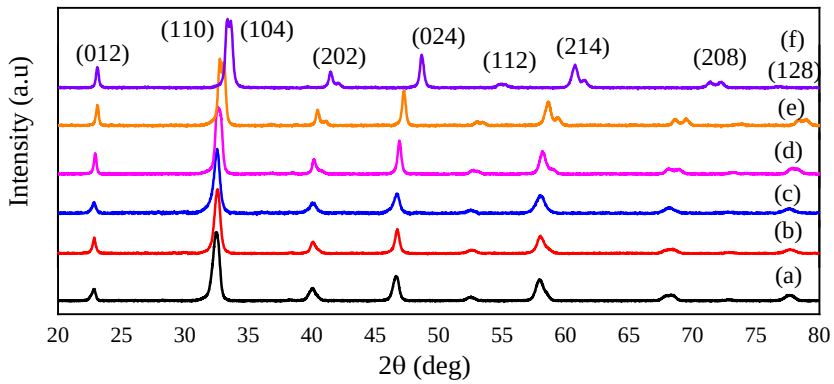

Figure 3-6 : X-ray diffraction diagrams of LMO-Co-x powders a) $LaMnO_3$, b) $LaMn_{0.8}Co_{0.2}O_3$, c) $LaMn_{0.6}Co_{0.4}O_3$, d) $LaMn_{0.4}Co_{0.6}O_3$, e) $LaMn_{0.2}Co_{0.8}O_3$, and f) $LaCoO_3$

Table 3-4 : X-ray characterization of LMO-Co-x powders

Sample Name	**X-Ray Fluorescence Spectroscopy**			**X-Ray Diffraction Spectroscopy**	
	La	**Mn**	**Co**	**Phase Structure**	**Crystalline Size (nm)**
LMO-Co-0.2	1	0.78	0.24	Cubic	24
LMO-Co-0.4	1	0.59	0.47	Cubic	20
LMO-Co-0.6	1	0.36	0.65	Rhombohedral	30
LMO-Co-0.8	1	0.19	0.89	Rhombohedral	30

The images containing surface morphology of the samples are given in Figure 3-7 and Figure 3-8. These SEM images show that sample have porous structure comprised of perovskite nanoparticles.

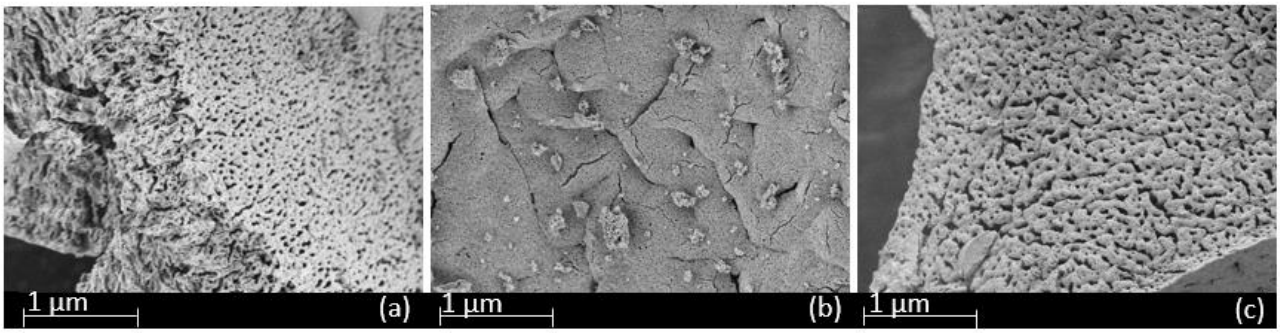

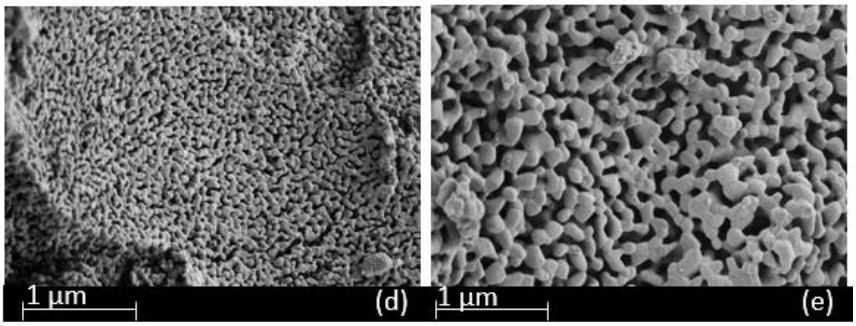

Figure 3-7 : SEM images of LTO-Co-x powders at 200 nm scale x: (a) 0.2, (b) 0.4, (c) 0.6, (d) 0.8, and (e) 1

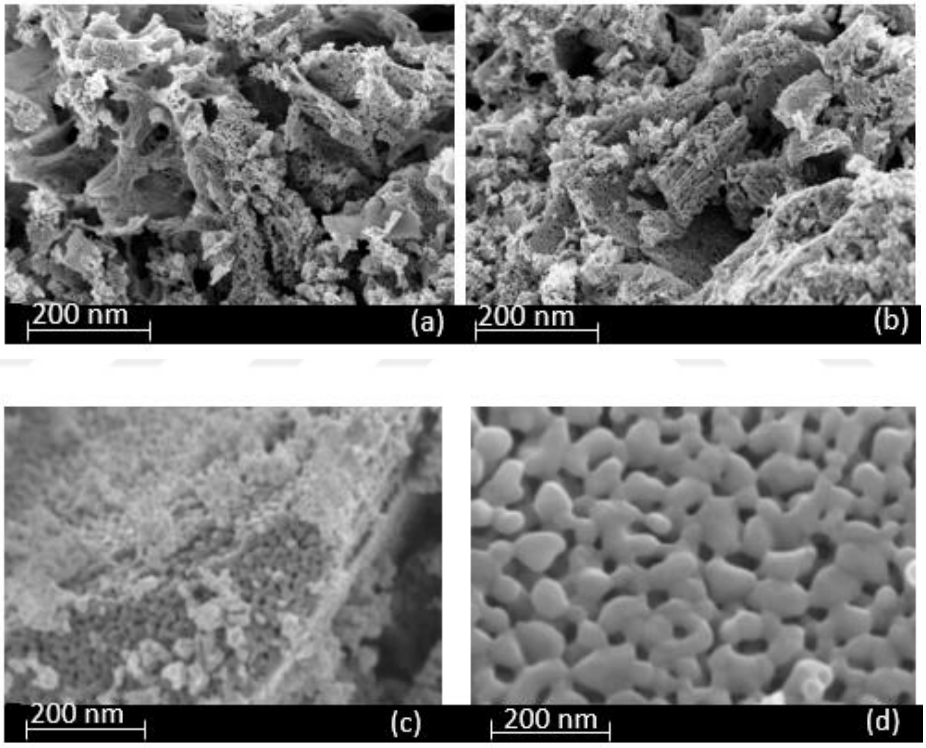

Figure 3-8 : SEM images of LMO-Co-x powders at 200 nm scale x : (a) 0.2, (b) 0.4, (c) 0.6, and (d) 0.8

3.1.3 $LaTi_{(1-x)}Fe_xO_3$ and $LaMn_{(1-x)}Fe_xO_3$ (x = 0, 0.2, 0.4, 0.6, 0.8, and 1)

X-ray diffraction diagrams of 20%, 40%, 60%, 80% Fe and 100% doped LTO phases were shown in Figure 3-9. The sharpness of the diffraction peaks indicates that a crystalline and pure structure was obtained. According to XRD diagrams, the La_2O_3 phase

is observed in 20% iron doped LTO sample. The samples, which had dopant of x ≥ 0.4, showed no impurities. When the diagrams were examined, the increase in the amount of Fe altered the crystal structure. LTO samples with 20%, 40%, 60% Fe doped were exhibited cubic structure (PDF 04-018-5557), LTO-Fe-0.8 and LFO were crystallized in orthorhombic structure (JCPSD No. 04-006-1884). With this change, peak positions shifted to slightly higher 2Θ values towards the $LaFeO_3$ structure. By changing the amount of additive, the amount of Fe element which was replacing Ti element had changed and the crystal size has changed accordingly. The crystal size was expected to increase as moved toward $LaFeO_3$ structure (Table 3-5). When the results of X-ray fluorescence spectroscopy were examined, it was seen that almost all targeted iron amount could be added to the structure (Table 3-5).

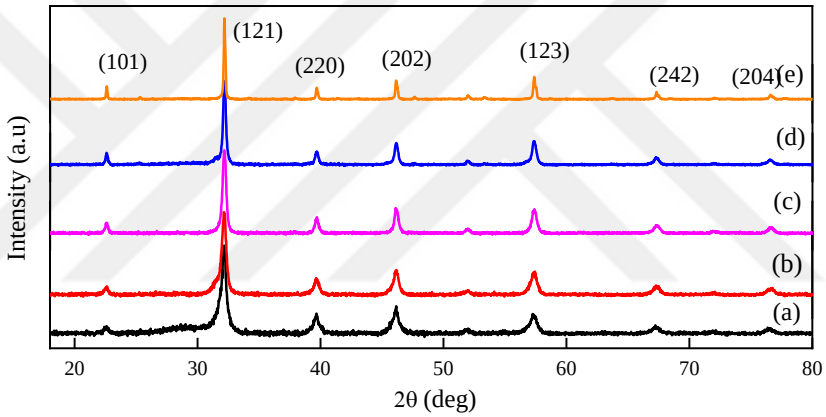

Figure 3-9 : X-ray diffraction diagrams of LTO-Fe-x powders (a) $LaTi_{0.8}Fe_{0.2}O_3$, (b) $LaTi_{0.6}Fe_{0.4}O_3$, (c) $LaTi_{0.4}Fe_{0.6}O_3$, (d) $LaTi_{0.2}Fe_{0.8}O_3$, and (e) $LaFeO_3$

Table 3-5 : X-ray characterization of LTO-Fe-x powders

Sample Name	**X-Ray Fluorescence Spectroscopy**			**X-Ray Diffraction Spectroscopy**	
	La	**Ti**	**Fe**	**Phase Structure**	**Crystalline Size (nm)**
LTO-Fe-0.2	1	0.59	0.19	Cubic	21
LTO-Fe-0.4	1	0.4	0.51	Cubic	22
LTO-Fe-0.6	1	0.33	0.58	Cubic	27
LTO-Fe-0.8	1	0.18	0.76	Orthorhombic	29
LFO	1		0.98	Orthorhombic	68

X-ray diffraction diagrams of 20%, 40%, 60%, 80% Fe and 100% doped LMO phases were shown in Figure 3-10. The sharpness of the diffraction peaks indicates that a crystalline and pure structure was obtained. According to XRD diagrams, all powders showed no impurities and crystal structure did not changed with the increase in the amount of. LMO-Fe-x powders exhibited cubic structure (PDF 04-018-5557). With this change, peak positions shifted to slightly lower 2Θ values towards the $LaFeO_3$ structure. When the results of X-ray fluorescence spectroscopy were examined, it was seen that almost all targeted iron amount could be added to the structure (Table 3-6).

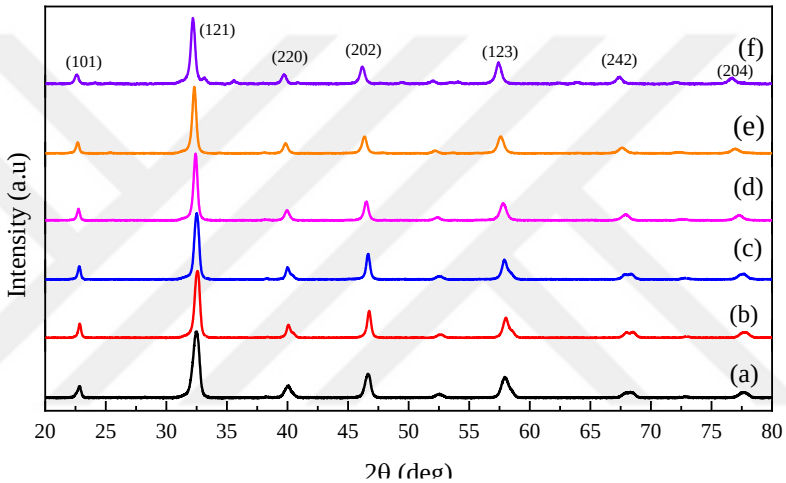

Figure 3-10 : X-ray diffraction diagrams of LMO-Fe-x powders (a) $LaMn_{0.8}Fe_{0.2}O_3$, (b) $LaMn_{0.6}Fe_{0.4}O_3$, (c) $LaMn_{0.4}Fe_{0.6}O_3$, (d) $LaMn_{0.2}Fe_{0.8}O_3$, and (e) $LaFeO_3$

Table 3-6 : X-ray characterization of LMO-Fe-x powders

Sample Name	**X-Ray Fluorescence Spectroscopy**			**X-Ray Diffraction Spectroscopy**	
	La	**Mn**	**Fe**	**Phase Structure**	**Crystalline Size (nm)**
LMO-Fe-0.2	1	0.72	0.19	Cubic	27
LMO-Fe-0.4	1	0.54	0.40	Cubic	27
LMO-Fe-0.6	1	0.37	0.61	Cubic	24
LMO-Fe-0.8	1	0.18	0.77	Cubic	22

The images containing surface morphology of the samples are given in Figure 3.11 and Figure 3-12. When the microstructure analysis was performed from the obtained images, it was seen that the samples had nanoparticle shape and porous structures except LMO-

Fe-0.6 and LMO-Fe-0.8. Increasing Fe dopant caused agglomeration and non-porous structure as seen in Figure 3-12.

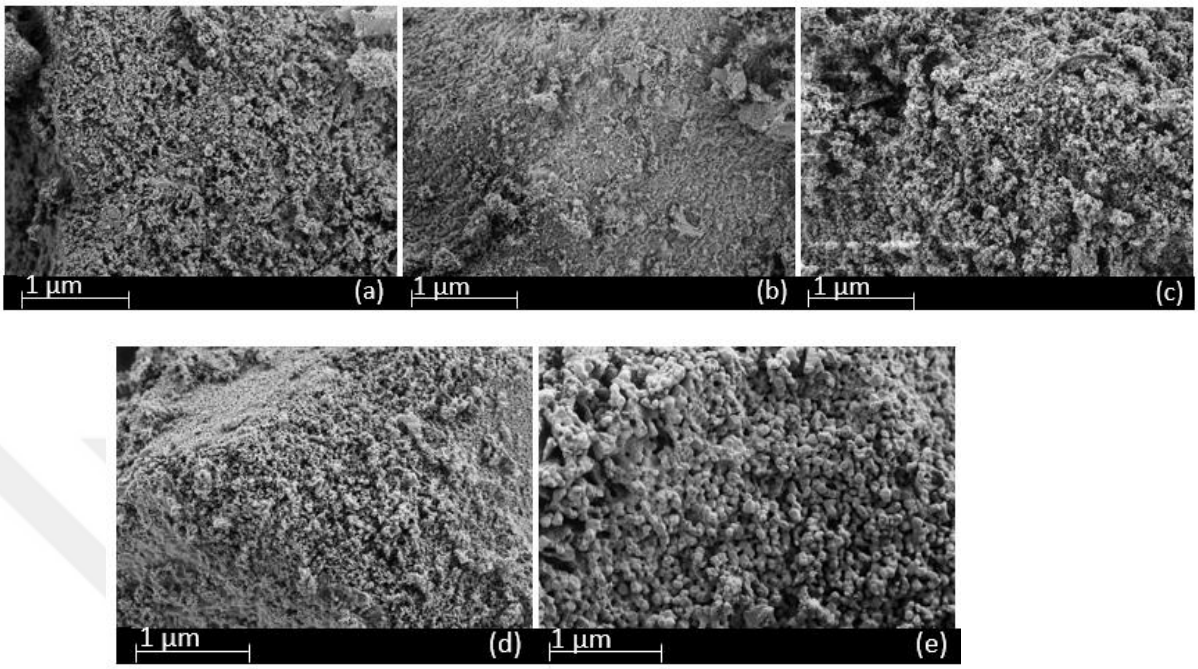

Figure 3-11 : SEM images of LTO-Fe-x powders at 200 nm scale x: (a) 0.2, (b) 0.4, (c) 0.6, (d), 0.8, and (e) 1

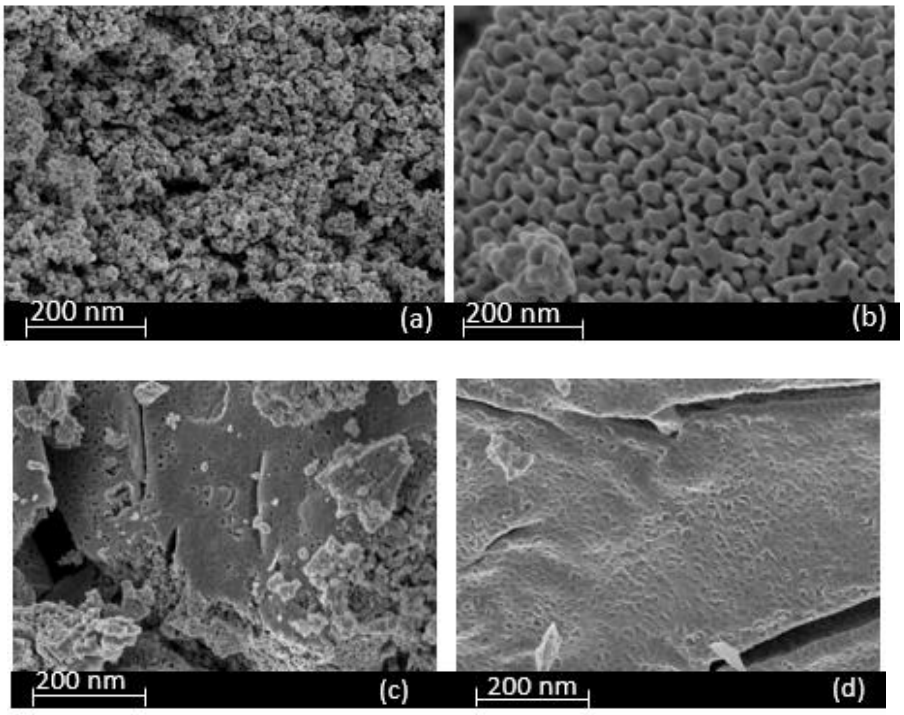

Figure 3-12 : SEM images of LMO-Fe-x powders at 200 nm scale x: (a) 0.2, (b) 0.4, (c) 0.6, and (d) 0.8

3.1.4 $La_{(1-x)}A_xTiO_3$ (A: Ca or Sr) and $La_{(1-x)}Ca_xMnO_3$

Figure 3-13 and Figure 3-14 show X-ray diffraction diagrams of 20%, 40%, 60%, 80% and 100% M (M: Ca or Sr) doped LTO powders and Figure 3-15 shows 10%, 30% and 50% doped LMO powders. The sharpness of the diffraction peaks indicates that a crystalline and pure structure was obtained. According to XRD diagrams for LTO powders, La_2O_3 phase was observed in the 20% Sr doped sample but not for Ca doped one. The samples, which had dopant of $x \geq 0.4$, showed no impurities. When the diagrams were examined, the increase in the amount of metal dopant do not affect the crystal structure of both LMO-Ca and LTO-Ca powders. LTO samples doped with Sr element showed cubic structure (PDF 04-007-0044), Ca element doped samples showed orthorhombic crystal structure (PDF 04-007-5451) and Ca element doped LMO samples showed cubic structure (JCPDS 04-020-5779). Also, peak positions shifted to slightly higher 2Θ values towards the $CaTiO_3$ and $CaMnO_3$ pure structures and lower 2Θ values towards the $SrTiO_3$ pure structure. By changing the amount of additive, the amount of metal element which was replacing La element had changed and the crystal size has changed accordingly. The crystal size was expected to increase as moved toward pure CTO structure and decrease as moved to CMO structure. (Table 3-7, Table 3-8, and Table 3-9).

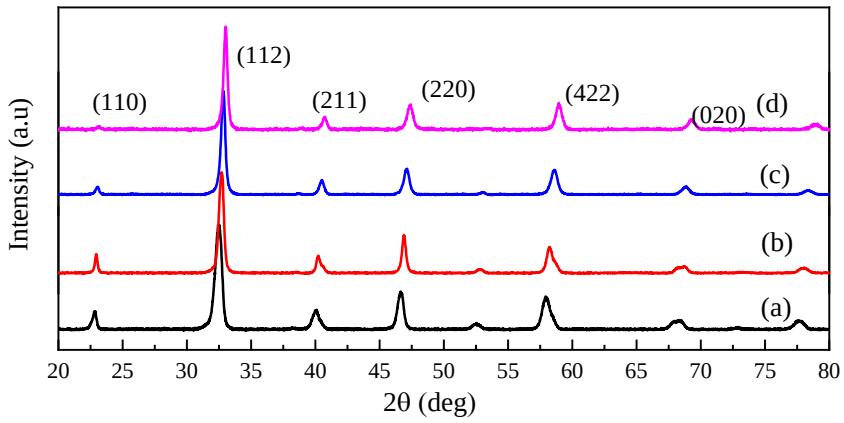

Figure 3-13 : X-ray diffraction diagrams of LMO-Ca-x powder (a) $LaMnO_3$, (b) $La_{0.9}Ca_{0.1}MnO_3$, (c) $La_{0.7}Ca_{0.3}MnO_3$, and (d) $La_{0.5}Ca_{0.5}MnO_3$

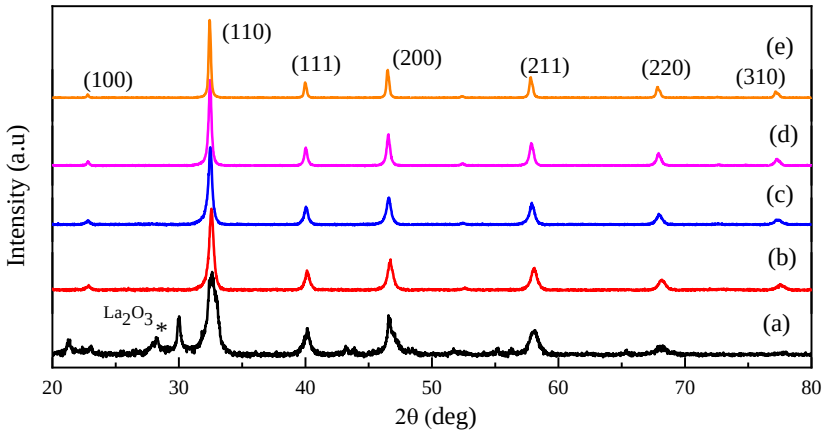

Figure 3-14 : X-ray diffraction diagrams of LTO-Sr-x powder (a) $La_{0.8}Sr_{0.2}TiO_3$, (b) $La_{0.6}Sr_{0.4}TiO_3$, (c) $La_{0.4}Sr_{0.6}TiO_3$, (d) $La_{0.2}Sr_{0.8}TiO_3$, and (e) $SrTiO_3$

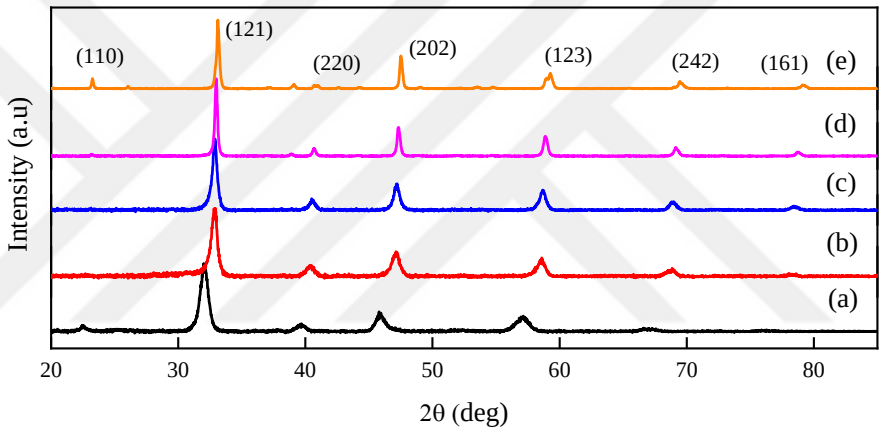

Figure 3-15 : X-ray diffraction diagrams of LTO-Ca-x powder (a) $La_{0.8}Ca_{0.2}TiO_3$, (b) $La_{0.6}Ca_{0.4}TiO_3$, (c) $La_{0.4}Ca_{0.6}TiO_3$, (d) $La_{0.2}Ca_{0.8}TiO_3$, and (e) $CaTiO_3$

When the results of X-ray fluorescence spectroscopy were examined, it was seen that almost all targeted metal contribution could be added to the structure and with the increasing metal dopant, crystal size changed. (Table 3-4, Table 3-5, and Table 3-6).

Table 3-7 : X-ray characterization of LTO-Sr-x powders

Sample Name	X-Ray Fluorescence Spectroscopy			X-Ray Diffraction Spectroscopy	
	La	Sr	Ti	Phase Structure	Crystalline Size (nm)
LTO-Sr-0.2	0.87	0.10	1	Cubic	15
LTO-Sr-0.4	0.55	0.34	1	Cubic	25
LTO-Sr-0.6	0.41	0.63	1	Cubic	28
LTO-Sr-0.8	0.19	0.79	1	Cubic	33
STO	-		1	Cubic	35

Table 3-8 : X-ray characterization of LTO-Ca-x powders

Sample Name	X-Ray Fluorescence Spectroscopy			X-Ray Diffraction Spectroscopy	
	La	Ca	Ti	Phase Structure	Crystalline Size (nm)
LTO-Ca-0.2	1	1	1	Orthorhombic	17
LTO-Ca-0.4	0.69	0.39	1	Orthorhombic	18
LTO-Ca-0.6	0.39	0.58	1	Orthorhombic	20
LTO-Ca-0.8	0.19	0.82	1	Orthorhombic	40
CTO	-		1	Orthorhombic	42

Table 3-9 : X-ray characterization of LMO-Ca-x powders

Sample Name	X-Ray Fluorescence Spectroscopy			X-Ray Diffraction Spectroscopy	
	La	Ca	Mn	Phase Structure	Crystalline Size (nm)
LMO-Ca-0.1	1	0.1	1	Cubic	27.4
LMO-Ca-0.3	0.7	0.3	1	Cubic	20.6
LMO-Ca-0.5	0.6	0.6	1	Cubic	19.2

The images containing surface morphology of the samples are given in Figure 3-15, Figure 3-16, and Figure 3-17. These SEM images show that sample have porous structure comprised of perovskite nanoparticles.

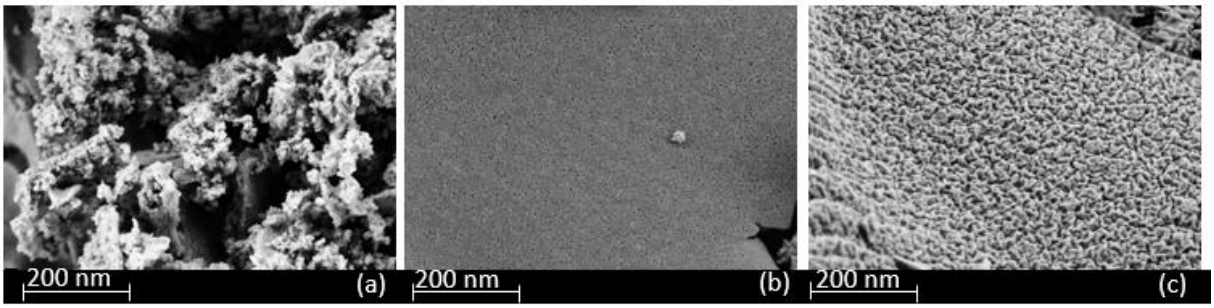

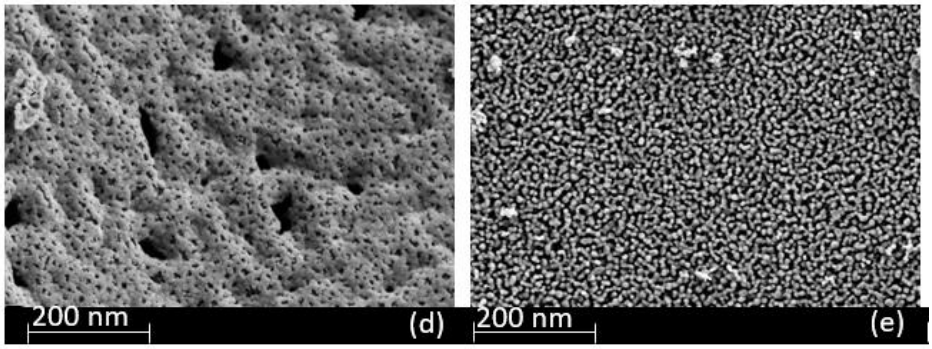

Figure 3-16 : SEM images of LTO-Sr-x powders at 200 nm scale x: (a) 0.2, (b) 0.4, (c) 0.6, (d) 0.8, and (e) 1

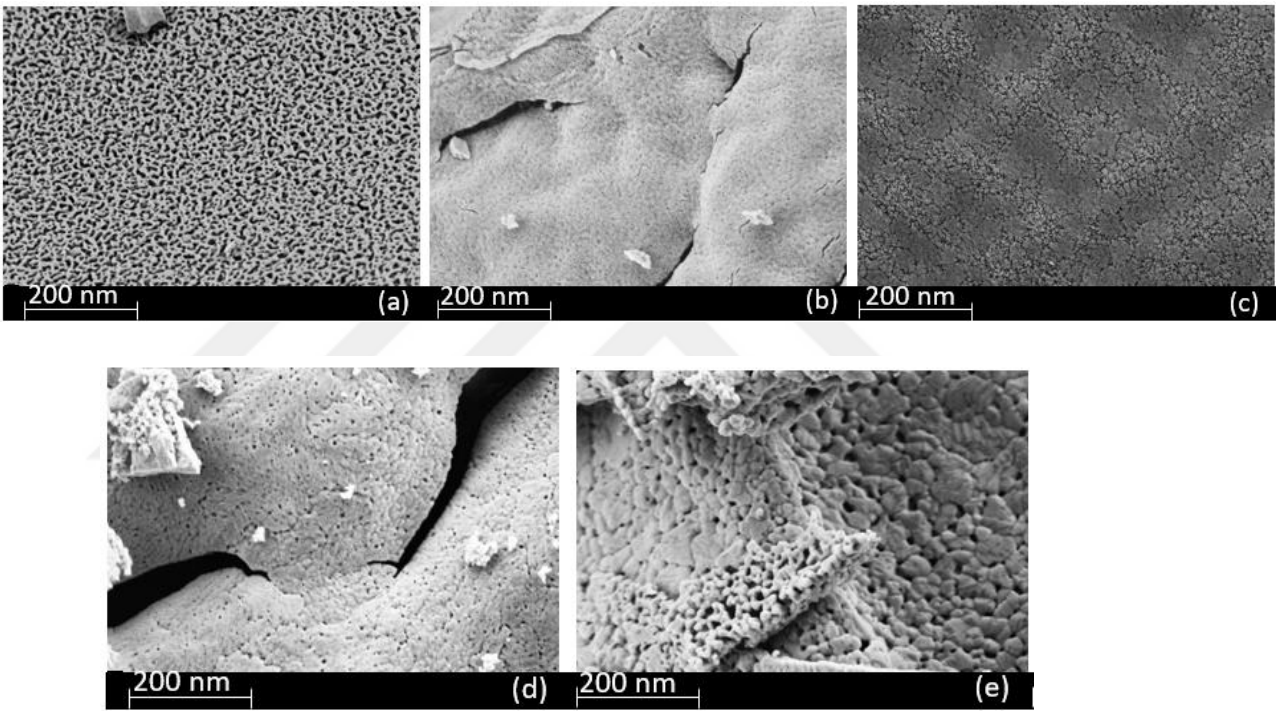

Figure 3-17 : SEM images of LTO-Ca-x powders at 200 nm scale x: (a) 0.2, (b) 0.4, (c) 0.6, (d) 0.8, and (e) 1

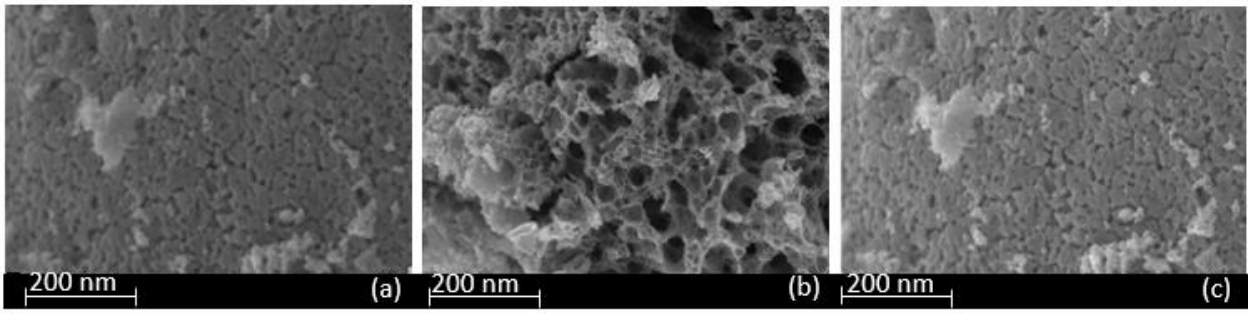

Figure 3-18 : SEM images of LMO-Ca-x powders at 200 nm scale x: (a) 0.1, (b) 0.3, and (c) 0.5

3.1.5 Ag doped $La_{0.2}Ca_{0.8}TiO_3$ and $SrTiO_3$ powder

XRD measurement proved that Ag metal was successfully doped in $SrTiO_3$ structure as seen in Figure 3-19. There were distinctive peaks that defines Ag ion and difference with the $SrTiO_3$.

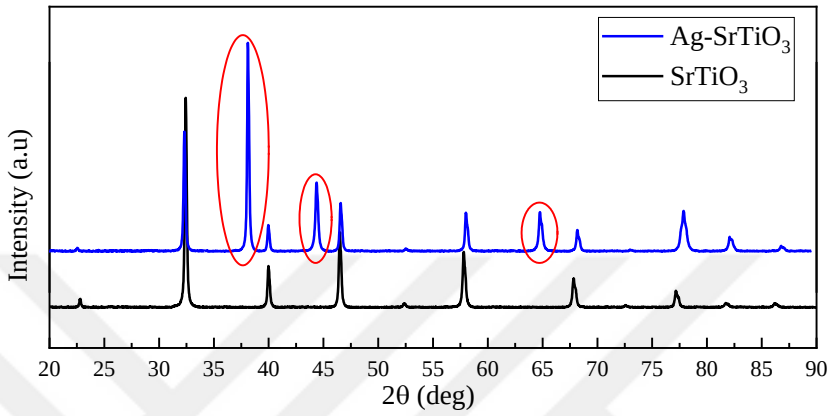

Figure 3-19 : XRD measurement results of $SrTiO_3$ and Ag doped $SrTiO_3$

XRD measurement proved that Ag metal was successfully doped in $La_{0.2}Ca_{0.8}TiO_3$ structure as seen in Figure 3-20. There were distinctive peaks that defines Ag ion and difference with the parental structure.

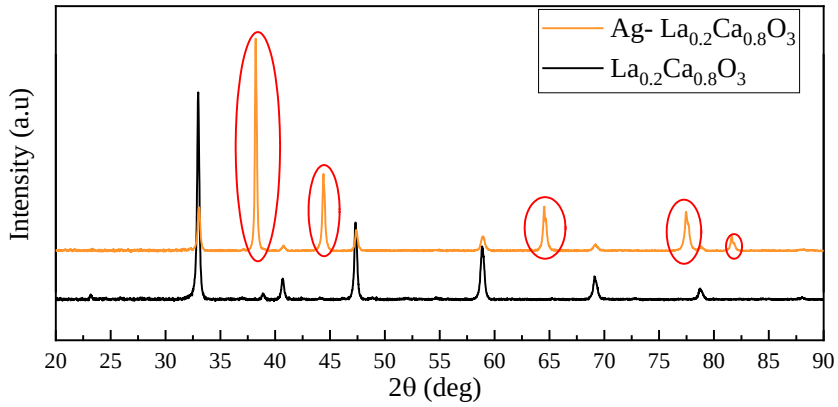

Figure 3-20 : XRD measurement results of $La_{0.2}Ca_{0.8}TiO_3$ and Ag doped $La_{0.2}Ca_{0.8}TiO_3$

3.2 *CO_2 Sensing Experiment Results*

Resistivity of LTO samples is too high for the determination range and even the values were in the range of the machine, very noisy measurement data was obtained. When temperature is applied, no change was observed.

Measurement data of LMO samples were much successful. Some materials did not show stable results at the beginning but with increasing temperature, more stable data was obtained.

Figure 3-21 shows the responses of different materials. Experiment started at room temperature while the dry air flow through the system with 2L/min and temperature was increased according the response of the material. Resistivity decreased with increasing temperature for the p-type materials.

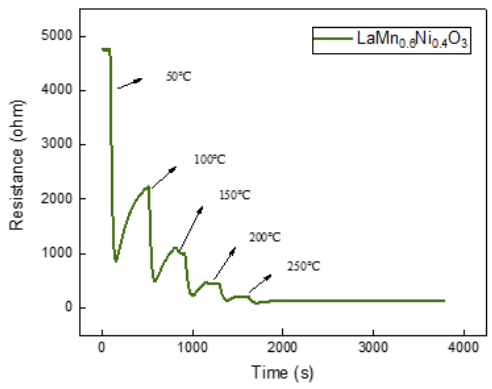

(a)

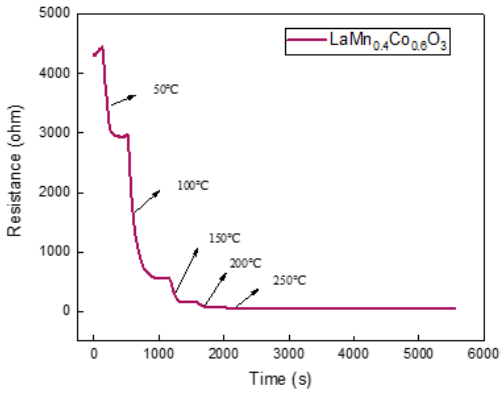

(b)

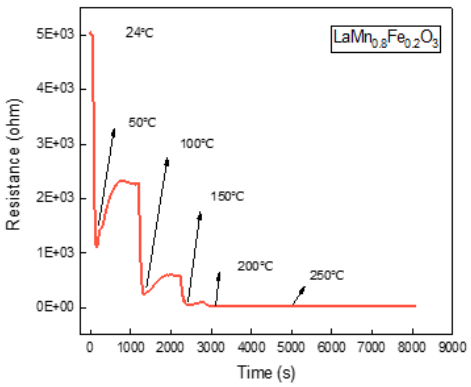

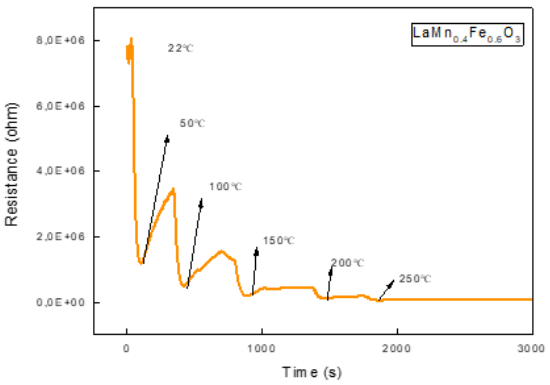

(c) (d)

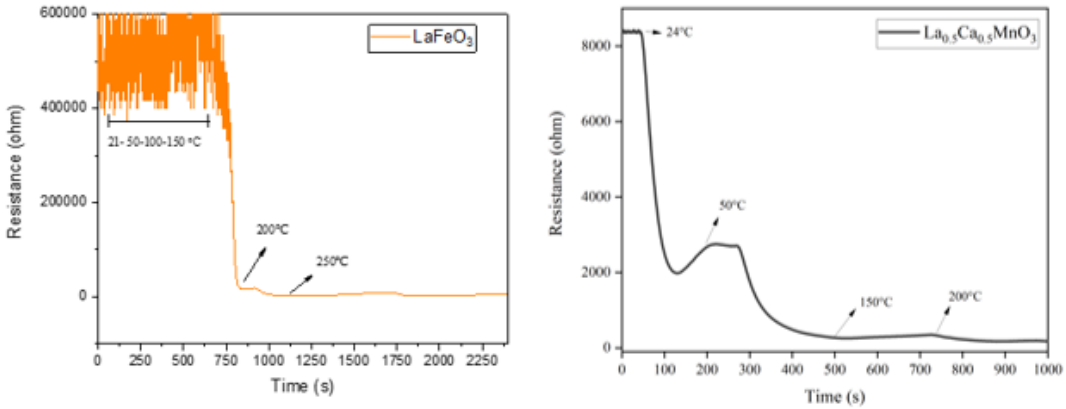

(e) (f)

Figure 3-21 : Resistance vs. time graph depending on the temperature change (a) $LaMn_{0.6}Ni_{0.4}O_3$, (b) $LaMn_{0.4}Co_{0.6}O_3$, (c) $LaMn_{0.8}Fe_{0.2}O_3$, (d) $LaMn_{0.4}Fe_{0.6}O_3$, (e) $LaFeO_3$, and (f) $La_{0.5}Ca_{0.5}MnO_3$

$LaNiO_3$ powder is n-type semiconductor on the contrary of the manganese containing powders. As seen in Figure 3-22, resistivity parallel to temperatures changes due to semiconductor behavior. This measurement was done under only dry air flowing at a speed of 2 L/min and starting temperature was 50 ^oC.

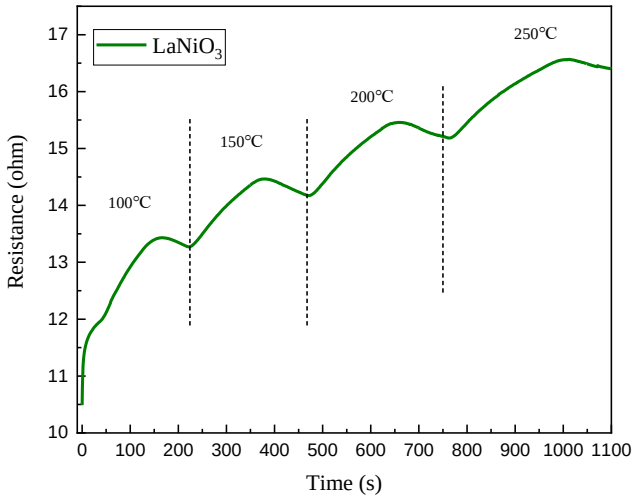

Figure 3-22 : Resistivity- time graph of $LaNiO_3$ coated sensor under dry air

However not every powder was suitable for the sensor application due to low conductivity. In Figure 3-23, very high and noisy resistance values can be seen.

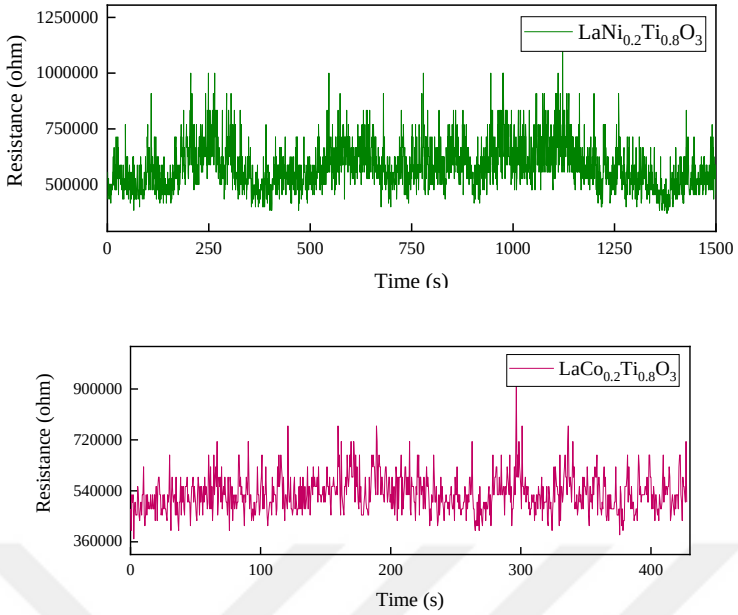

Figure 3-23 : Experimental results of LTO-Ni-0.2 and LTO-Co-0.2 powders

$La_{0.2}Ca_{0.8}TiO_3$ and SrTiO3 coated sensors also gave results like LTO-Ni-0.2 and LTO-Co-0.2 powders. For reducing resistivity, highly conductive Ag metal were chosen and doped to these powders. After that sensor fabrication and sensing measurement were done. Successful doping of Ag metal affected positively, and resistance values were decreased after specific temperature as in Figure 3-24. These temperatures were 250 ºC and 150 ºC for Ag-LTO-Ca-0.8 and Ag-STO, respectively.

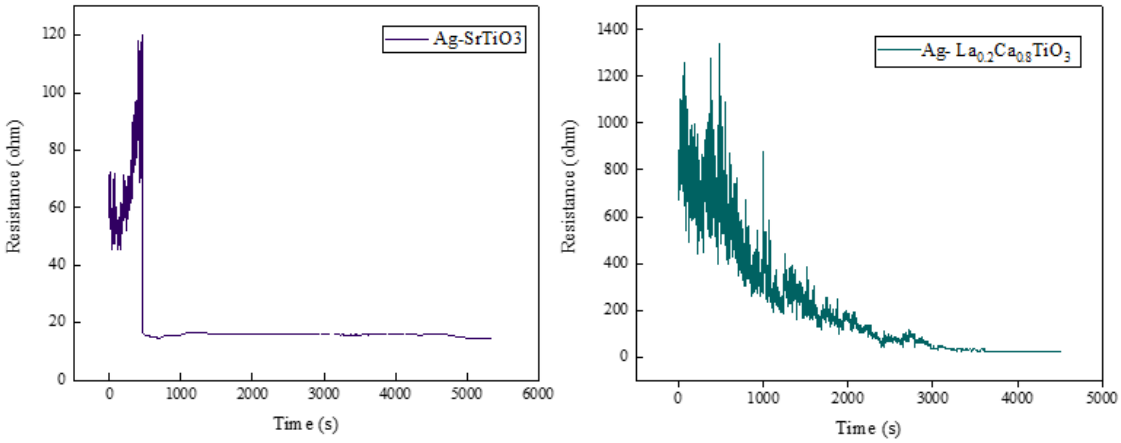

Figure 3-24 : Resistivity- time graph of Ag-LTO-Ca-0.8 and Ag-STO coated sensor under dry air

After the stabilization of the air flow and temperature, CO_2 gas was opened and closed with different time intervals and concentrations to see response and recovery time of the sensor. Different air flow speeds were used to understand the mechanism of the sensing behavior. As shown in Figure 3-25, respond of the material differed with the flow speed.

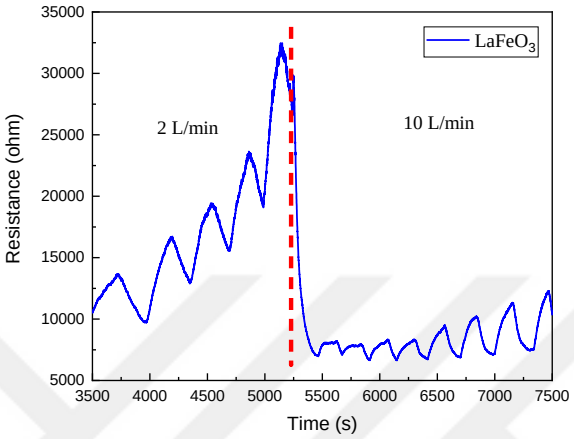

Figure 3-25 : Different gas flows for $LaFeO_3$ powder (I) 2L/min and (II) 10L/min

In Figure 3-25, CO_2 gas flow started at 3500. second with 2L/min speed and continued until the 5000. second. After this point, CO_2 flow was stopped, and speed of dry air flow was set to 10L/min and sharp decreased was monitored as seen in graph. It was able to stabilize after 500 s. Then, CO_2 gas was opened again. Figure 3-26 shows detailly both parts.

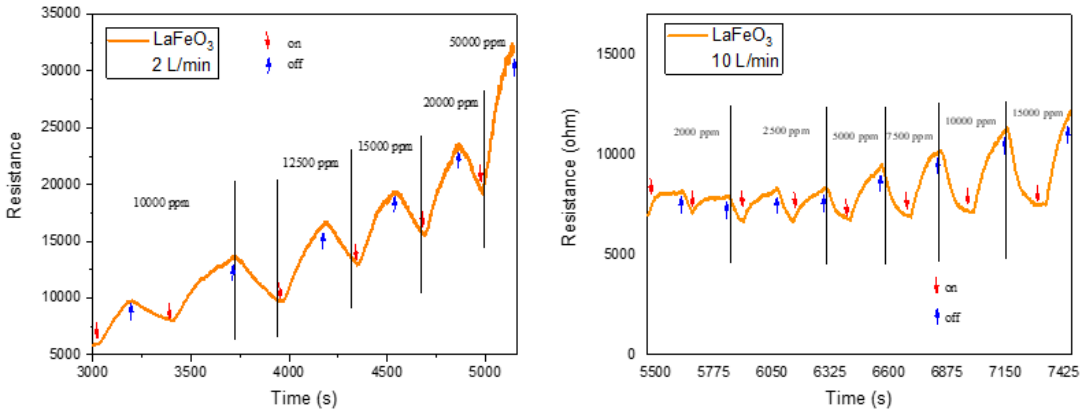

Figure 3-26 : 2 L/min dry air flow vs. 10 L/min dry flow air graphs at 250 ^oC while CO_2 gas flowing

At both speeds, when CO_2 gas was flowing through the system, resistivity increased and with increasing gas concentration, this resistivity change expanded. However faster flow speed gave more stable and continues results. This behavior can be explained with the sensing mechanism. CO_2 gas interacted with the surface oxygen and metal which can be called as active site. Also, there was oxygen atoms previously bonded on the surface. When dry air flows faster, these previously bonded oxygens were wiped away from the surface and allow CO_2 molecule to bond more places on the surface. Moreover, respond and recovery time were shorter due to this effect.

CO_2 gas concentration effect was investigated. Results showed that powders react with CO_2 gas but not enough to sense it properly. Figure 3-27 and Figure 3-28 shows some examples gas passing through with different concentrations.

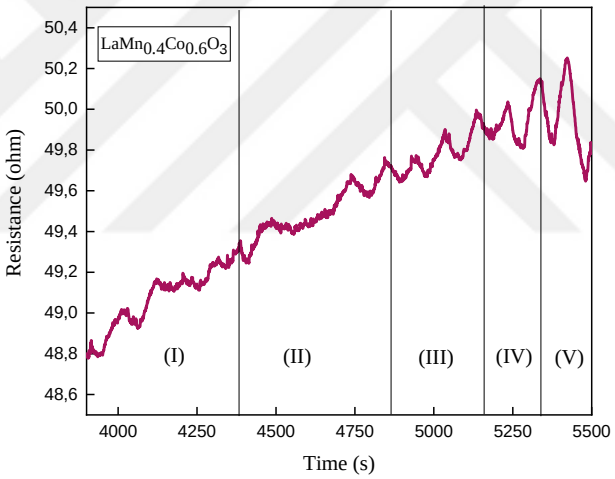

Figure 3-27 : Different CO_2 gas concentrations (I) 50000 ppm, (II) 75000 ppm, (III) 100000 ppm, (IV) 250000 ppm, and (V) 500000 ppm

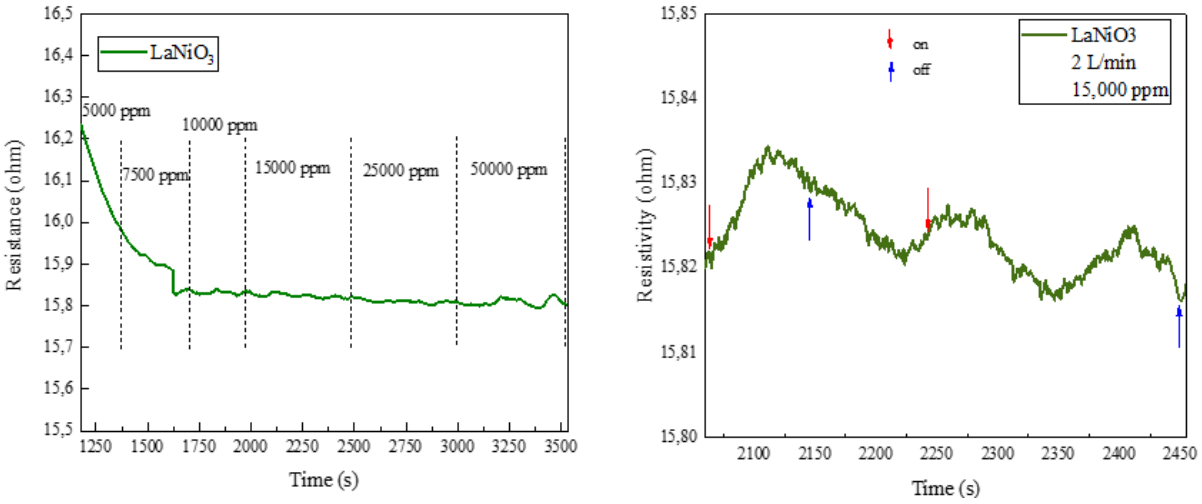

Figure 3-28 : $LaNiO_3$ coated sensor measurement while CO_2 gas flowing through

According to the above figures, a specific pattern could not determine. Shorter exposure to the gas does not give good results. Generally, lower ppm concentrations (500 to 7500) were hard to detect with at present system which give rise to thought, sensors had insufficient sensitivity.

Chapter 4:

CONCLUSION AND FUTURE PERSPECTIVES

In this thesis, ABO_3 type perovskites were investigated for CO_2 gas sensing application. Sol-gel method was used for synthesis of powders. Calcination temperature of prepared $LaMnO_3$ based perovskites was determined as 700^oC according to XRD analysis results and calcination temperature of prepared $LaTiO_3$ based perovskites was determined as 900^oC. Under these temperatures, impurities were detected in their structure.

$LaTiO_3$ based materials show no change during the sensing measurements due to their insufficient conductivity. In order to improve the conductivity of powders, highly conductive Ag metal was doped to powders.

LMO based powders gave respond at lower temperatures when compared to LTO based powders. LTO based powders may give respond at higher temperatures like 400-600 ^oC. Electrode with the Pt heater may try to reach these high temperatures without heating the whole system.

Exposure time can be increased and be monitored its effects. The chamber with the smaller volume can be used to be sure the whole gas is flowing on the sensor. Thinner films may prepare to increase sensitivity.

To better understand the sensing mechanism, Raman measurements can be used. While gas flowing, occurrence of the changes in the bonding can be observed. Also, the gas mixture, which is leaving the system, can be measured with gas chromatography to determine quantity of real sensed and bonded gas.

BIBLIOGRAPHY

[1] P. Lightfoot and R. E. Morris, “Perovskites,” *J. Chem. Soc. Dalt. Trans.*, p. 1772, 2015.

[2] J. Zhu *et al.*, “Perovskite oxides: Preparation, characterizations, and applications in heterogeneous catalysis,” *ACS Catal.*, vol. 4, no. 9, pp. 2917–2940, 2014.

[3] Z. Cheng and J. Lin, “Layered organic-inorganic hybrid perovskites: Structure, optical properties, film preparation, patterning and templating engineering,” *CrystEngComm*, vol. 12, no. 10, pp. 2646–2662, 2010.

[4] E. Abdul and R. Assirey, “Perovskite synthesis , properties and their related biochemical and industrial application,” *Saudi Pharm. J.*, vol. 27, no. 6, pp. 817–829, 2019.

[5] M. A. Peña and J. L. G. Fierro, “Chemical structures and performance of perovskite oxides,” *Chem. Rev.*, vol. 101, no. 7, pp. 1981–2017, 2001.

[6] S. C. Tidrow, “Mapping comparison of goldschmidt’s tolerance factor with perovskite structural conditions,” *Ferroelectrics*, vol. 470, no. 1, pp. 13–27, 2014.

[7] P. Kanhere and Z. Chen, “A review on visible light active perovskite-based photocatalysts,” *Molecules*, vol. 19, no. 12, pp. 19995–20022, 2014.

[8] N. F. Atta, A. Galal, and E. H. El-Ads, “Perovskite Nanomaterials – Synthesis, Characterization, and Applications,” *Perovskite Mater. - Synth. Characterisation, Prop. Appl.*, pp. 107–151, 2016.

[9] R. Shi, G. I. N. Waterhouse, and T. Zhang, “Recent Progress in Photocatalytic CO2 Reduction Over Perovskite Oxides,” *Sol. RRL*, vol. 1, no. 11, pp. 1–17, 2017.

[10] T. Ishihara and T. Properties, “Inorganic Perovskite Oxides,” in *Springer Handbook of Electronic and Photonic Materials*, no. Iv, Springer, Cham, 2017, pp. 1405–1420.

[11] H. Tanaka, “An intelligent catalyst: The self-regenerative palladium-perovskite catalyst for automotive emissions control,” *Catal. Surv. from Asia*, vol. 9, no. 2, pp. 63–74, 2005.

[12] N. Labhasetwar *et al.*, “Perovskite-type catalytic materials for environmental applications Perovskite-type catalytic materials for environmental applications,”

Sci. Technol. Adv. Mater., vol. 16, no. 3, pp. 1–13, 2015.

[13] D. D. Athayde *et al.*, "Review of perovskite ceramic synthesis and membrane preparation methods," *Ceram. Int.*, vol. 42, no. 6, pp. 6555–6571, 2016.

[14] Y. Dimitriev, Y. Ivanova, and R. Iordanova, "History of Sol-Gel Science and Technology," *ChemInform*, vol. 40, no. 12, pp. 181–192, 2009.

[15] A. E. Danks, S. R. Hall, and Z. Schnepp, "The evolution of 'sol-gel' chemistry as a technique for materials synthesis," *Mater. Horizons*, vol. 3, no. 2, pp. 91–112, 2016.

[16] A. P. Wilkinson, "Solid State Synthesis Methods," *Chem*, vol. 6182, pp. 1–17, 2001.

[17] U. P. M. Ashik, S. Kudo, and J. Hayashi, *An Overview of Metal Oxide Nanostructures*. Elsevier Ltd., 2018.

[18] Ö. ECE, "HYDROTHERMAL SYNTHESIS AND STRUCTURAL CHARACTERIZATION OF OPEN- FRAMEWORK METAL PHOSPHATES TEMPLATED WITH ORGANIC DIAMINES A Thesis Submitted to," no. July, 2012.

[19] "Introduction To Perovskite Structured Materials," 1856, pp. 28–65.

[20] S. K. Sahoo, B. Manoharan, and N. Sivakumar, "Introduction: Why perovskite and perovskite solar cells?," in *Perovskite Photovoltaics: Basic to Advanced Concepts and Implementation*, Elsevier Inc., 2018, pp. 1–24.

[21] G. Neri, "First Fifty Years of Chemoresistive Gas Sensors," *Chemosensors*, vol. 3, no. 1, pp. 1–20, 2015.

[22] J. B. Balaguru RJ, "Mimic of a Gas sensor, Metal Oxide Gas Sensing Mechanism, Factors Influencing the Sensor Performance and Role of nanomaterials based gas sensors," *NPTEL–Electrical Electron. Eng. Nanodevices*, pp. 1–30, 2004.

[23] N. Yamazoe and K. Shimanoe, "1 - Fundamentals of semiconductor gas sensors," in *From plant genomics to plant biotechnology*, Woodhead Publishing Limited, 2013, pp. 3–34.

[24] K. S. Noboru Yamazoe, "Basic approach to the transducer function of oxide semiconductor gas sensors," *Sensors Actuators B*, no. 160, pp. 1352–1362, 2011.

[25] Figaro Engineering, "Operating principle - electrochemical type." [Online]. Available: https://www.figaro.co.jp/en/technicalinfo/principle/electrochemical-

type.html.

[26] ProOxygen, “Annual CO2,” 2019. [Online]. Available: https://www.co2.earth/annual-co2.

[27] UIG, “Universal Industrial Gases, Inc.,” 2017. [Online]. Available: http://www.uigi.com/h2_conv.html.

[28] “Climate Change_ Atmospheric Carbon Dioxide _ NOAA Climate.” .

[29] G. F. Fine, L. M. Cavanagh, A. Afonja, and R. Binions, “Metal oxide semi-conductor gas sensors in environmental monitoring,” *Sensors*, vol. 10, no. 6, pp. 5469–5502, 2010.

[30] NOAA, “What is the carbon cycle?,” 2019. [Online]. Available: https://oceanservice.noaa.gov/facts/carbon-cycle.html#:~:text=When new life is formed,atmosphere over and over again.

[31] Y. F. Sun *et al.*, “Metal oxide nanostructures and their gas sensing properties: A review,” *Sensors*, vol. 12, no. 3, pp. 2610–2631, 2012.

[32] A. W. Bott, “Electrochemistry of Semiconductors,” *Curr. Seperation*, vol. 17, no. 3, pp. 87–91, 1998.

[33] Z. Zhang and J. T. Yates, “Band bending in semiconductors: Chemical and physical consequences at surfaces and interfaces,” *Chem. Rev.*, vol. 112, no. 10, pp. 5520–5551, 2012.

[34] C. Wang, L. Yin, L. Zhang, D. Xiang, and R. Gao, “Metal oxide gas sensors: Sensitivity and influencing factors,” *Sensors*, vol. 10, no. 3, pp. 2088–2106, 2010.

[35] X. F. Wang, W. Ma, X. Z. Song, and J. F. Hu, “A theoretical insight into CO2 sensing performance on the orthorhombic LaMnO3 (0 1 0) surface,” *Chem. Phys. Lett.*, vol. 687, pp. 138–142, 2017.

[36] L. Q. Jun, G. W. Bin Djaswadi, H. F. Bin Hawari, and M. A. B Zakariya, “Simulation of Interdigitated Electrodes (IDEs) Geometry Using COMSOL Multiphysics,” *Int. Conf. Intell. Adv. Syst. ICIAS 2018*, pp. 1–6, 2018.

[37] S. Coating and S. C. Guide, “Spin Coating : A Guide to Theory and Techniques Introduction to Spin Coating,” 2016. .

[38] B. Ferrari and R. Moreno, “EPD kinetics: A review,” *Journal of the European Ceramic Society*, vol. 30, no. 5. pp. 1069–1078, 2010.

[39] M. Eslamian and F. Soltani-Kordshuli, “Development of multiple-droplet drop-

casting method for the fabrication of coatings and thin solid films," *J. Coatings Technol. Res.*, vol. 15, no. 2, pp. 271–280, 2018.

[40] A. T. Dan and S. Mutlu, "MetalOksitİncFilmlerin Gaz Sensörü Investigation of Gas Sensing Applications of," 2014.

[41] V. R. Shinde, T. P. Gujar, and C. D. Lokhande, "Enhanced response of porous ZnO nanobeads towards LPG: Effect of Pd sensitization," *Sensors Actuators, B Chem.*, vol. 123, no. 2, pp. 701–706, 2007.

[42] V. E. Bochenkov and G. B. Sergeev, "Sensitivity , Selectivity , and Stability of Gas-Sensitive Metal-Oxide Nanostructures," in *Metal Oxide Nanostructures and their applications*, vol. 3, Y.-B. H. A. Umar, Ed. American Scientific Publishers, 2010, pp. 31–52.

[43] G. Korotcenkov, "Metal oxides for solid-state gas sensors: What determines our choice?," *Mater. Sci. Eng. B Solid-State Mater. Adv. Technol.*, vol. 139, no. 1, pp. 1–23, 2007.

[44] M. Fleischer and H. Meixner, "Selectivity in high-temperature operated semiconductor gas-sensors," *Sensors Actuators, B Chem.*, vol. 52, no. 1–2, pp. 179–187, 1998.

[45] H. J. Kim and J. H. Lee, "Highly sensitive and selective gas sensors using p-type oxide semiconductors: Overview," *Sensors Actuators, B Chem.*, vol. 192, pp. 607–627, 2014.

[46] P. K. M. Al-Aubidy, "Sensor Characteristics." .

[47] R. K. W. Peter E. J. Flewitt, *Physical Methods for Material Characterization*. 1994.

[48] B. Fultz and J. Howe, "Diffraction and the X-Ray Powder Diffractometer," in *Transmission Electron Microscopy and Diffractometry of Materials 4th Ed*, 4th ed., 2013, p. 761.

[49] S. R. C. Douglas A. Skoog, F. James Holler, "Principles of Instrumental Analysis," *J. Chem. Educ.*, vol. 69, no. 8, p. A224, Aug. 1992.

[50] des S. et des T. N. Bounakhla, Moussa (Centre National de l'Energie and des S. et des T. N.) Tahri, Mounia (Centre National de l'Energie, "X-Ray Fluorescence Analytical Techniques." pp. 1–83.

[51] W. Zhou, R. Apkarian, Z. L. Wang, and D. Joy, "Fundamentals of scanning electron microscopy (SEM)," *Scanning Microsc. Nanotechnol. Tech. Appl.*, pp.

1–40, 2007.

[52] U. of Utah, “Lecture 3 :Brief Overview of Traditional Microscopes,” pp. 1–50, 2009.

[53] M. Afzal, P. S. Naik, and L. I. Nadaf, “Cost Effective Experimental Setup for Gas Sensing Applications,” *IOSR J. Appl. Chem.*, vol. 8, no. 12, pp. 37–44, 2015.

VITA

Zeynep Sena Kulaksız was born in Istanbul, Turkey in 1994. She finished Umraniye Anatolian High School, Istanbul, in 2012. She received her BSc degree in Chemistry from Istanbul Technical University, Istanbul, in January 2018. In February 2018, she started her master studies in Chemistry at Koç University and joined Functional Materials Research Group under supervision of Assoc. Prof. Uğur Ünal.